Diederik Depla
Stijn Mahieu
Editors

SPRINGER SERIES IN MATERIALS SCIENCE 109

Reactive Sputter Deposition

Springer Series in
MATERIALS SCIENCE 109

Springer Series in
MATERIALS SCIENCE

Editors: R. Hull R. M. Osgood, Jr. J. Parisi H. Warlimont

The Springer Series in Materials Science covers the complete spectrum of materials physics, including fundamental principles, physical properties, materials theory and design. Recognizing the increasing importance of materials science in future device technologies, the book titles in this series reflect the state-of-the-art in understanding and controlling the structure and properties of all important classes of materials.

99 **Self-Organized Morphology in Nanostructured Materials**
Editors: K. Al-Shamery and J. Parisi

100 **Self Healing Materials**
An Alternative Approach to 20 Centuries of Materials Science
Editor: S. van der Zwaag

101 **New Organic Nanostructures for Next Generation Devices**
Editors: K. Al-Shamery, H.-G. Rubahn, and H. Sitter

102 **Photonic Crystal Fibers**
Properties and Applications
By F. Poli, A. Cucinotta, and S. Selleri

103 **Polarons in Advanced Materials**
Editor: A.S. Alexandrov

104 **Transparent Conductive Zinc Oxide**
Basics and Applications in Thin Film Solar Cells
Editors: K. Ellmer, A. Klein, and B. Rech

105 **Dilute III-V Nitride Semiconductors and Material Systems**
Physics and Technology
Editor: A. Erol

106 **Into The Nano Era**
Moore's Law Beyond Planar Silicon CMOS
Editor: H.R. Huff

107 **Organic Semiconductors in Sensor Applications**
Editors: D.A. Bernards, R.M. Ownes, and G.G. Malliaras

108 **Evolution of Thin-Film Morphology**
Modeling and Simulations
By M. Pelliccione and T.-M. Lu

109 **Reactive Sputter Deposition**
Editors: D. Depla amd S. Mahieu

110 **The Physics of Organic Superconductors and Conductors**
Editor: A. Lebed

Volumes 50–98 are listed at the end of the book.

D. Depla S. Mahieu
Editors

Reactive Sputter Deposition

With 341 Figures

Professor Dr. Diederik Depla
Dr. Stijn Mahieu
Gent University, Department of Solid-State Sciences
281-S1 Krijgslaan, 9000 Gent, Belgium
E-mail: diederik.depla@ugent.be, stijn.mahieu@ugent.be

Series Editors:

Professor Robert Hull
University of Virginia
Dept. of Materials Science and Engineering
Thornton Hall
Charlottesville, VA 22903-2442, USA

Professor Jürgen Parisi
Universität Oldenburg, Fachbereich Physik
Abt. Energie- und Halbleiterforschung
Carl-von-Ossietzky-Strasse 9–11
26129 Oldenburg, Germany

Professor R. M. Osgood, Jr.
Microelectronics Science Laboratory
Department of Electrical Engineering
Columbia University
Seeley W. Mudd Building
New York, NY 10027, USA

Professor Hans Warlimont
Institut für Festkörper-
und Werkstofforschung,
Helmholtzstrasse 20
01069 Dresden, Germany

ISSN 0933-033X

ISBN 978-3-540-76662-9 Springer Berlin Heidelberg New York

Library of Congress Control Number: 2007938637

All rights reserved.
No part of this book may be reproduced in any form, by photostat, microfilm, retrieval system, or any other means, without the written permission of Kodansha Ltd. (except in the case of brief quotation for criticism or review.)
This work is subject to copyright. All rights are reserved, whether the whole or part of the material is concerned, specifically the rights of translation, reprinting, reuse of illustrations, recitation, broadcasting, reproduction on microfilm or in any other way, and storage in data banks. Duplication of this publication or parts thereof is permitted only under the provisions of the German Copyright Law of September 9, 1965, in its current version, and permission for use must always be obtained from Springer. Violations are liable to prosecution under the German Copyright Law.

Springer is a part of Springer Science+Business Media.
springer.com

© Springer-Verlag Berlin Heidelberg 2008

The use of general descriptive names, registered names, trademarks, etc. in this publication does not imply, even in the absence of a specific statement, that such names are exempt from the relevant protective laws and regulations and therefore free for general use.

Typesetting: Data prepared by SPi using a Springer LaTeX macro package
Cover concept: eStudio Calamar Steinen
Cover production: WMX Design GmbH, Heidelberg

Printed on acid-free paper SPIN: 12067657 57/3180/SPi 5 4 3 2 1 0

Preface

The most straightforward method to change the surface properties of a material is to deposit a thin film or coating on it. Hence, it is not surprising that an overwhelming amount of scientific and technical papers is published each year on this topic. Sputter deposition is one of the many so-called physical vapour deposition (PVD) techniques. In most cases, sputter deposition uses a magnetically enhanced glow discharge or magnetron discharge to produce the ions which bombard and sputter the cathode material. In the first chapter of this book (Chap. 1), the details of the sputter process are discussed. Essential to sustain the discharge is the electron emission during ion bombardment. Indeed, the emitted electrons are accelerated from the target and can ionize gas atoms. The formed ions bombard again the target completing the sustaining process. A complete chapter is assigned to this process to highlight its importance (Chap. 2). Although the sustaining process can be described quite straightforward, a complete understanding of the magnetron discharge and the influence of different parameters on the discharge characteristics is only possible by modelling (see Chap. 3). With these three chapters, the reader should be able to form an idea of the target and plasma processes occurring during a DC magnetron discharge.

When a reactive gas is added to the discharge, it becomes possible to deposit compound materials. This process is called *reactive sputter deposition*. The changes of the deposition process as a function of the reactive gas addition are discussed in Chaps. 4 and 5. The former (Chap. 4) describes the well-known "Berg" model, which enables a better understanding of the general aspects of reactive magnetron sputtering. The next chapter (Chap. 5) summarizes several experimental results and shows the need to more detailed models to describe the reactive sputtering process.

One of the major problems of the reactive sputter process is its complexity and several fundamental aspects of the process have not been elucidated yet. Only by understanding all its details, it is possible to understand the properties of the obtained thin film as a function of the deposition conditions. In this respect, it is necessary to describe the deposition flux towards

the substrate. This can be achieved by modelling the transport of sputtered particles towards the substrate (Chap. 6). However, not only the metallic flux but also the energy flux towards the substrate is important. This latter forms the subject of the following chapter (Chap. 7). More details of the reactive magnetron sputter process can be achieved by a good knowledge of the available plasma diagnostic tools. Hence, they form the content of the next two chapters (Chaps. 8 and Chap. 9). A nice illustration of the implementation of these tools is shown in the Chap. 10 which demonstrates their use in the study of the cross-corner and cross-magnetron effect (Chap. 10).

Finally, the book ends with some interesting examples of materials deposited with reactive sputter deposition. Indeed, complex materials such as solid electrolytes (Chap. 11), complex oxides (Chap. 12) and electrochromic thin films (Chap. 13). In the last chapter, the reader can learn more about the simulation of the growth of thin film deposited by magnetron sputtering (Chap. 14).

Although the technique is easy to use, it conceals enough challenges to remain scientific interesting. This explains its popularity in the academic world. Also in the industrial world, reactive magnetron sputtering remains an interesting and often used technique, due to its flexibility and scalability and has gained in this way a strong position for large-area deposition of thin films. As for most thin film deposition techniques, sputter deposition was once considered a black art and only in the last two decades, there has been a vast increase in the range of material types which can be deposited, the complexity of thin films which are possible, the ability to deposit precisely controlled heterostructures and the reproducibility of film deposition. The origin of this change is the trend to analyse in more detail all relevant processes during the thin film deposition to maximize the level of control. This forms exactly the goal of this book, i.e. to give the reader on overview of the important processes during sputter deposition and of the aim to describe them by modelling and to use them to deposit complex materials such as perovskite, solid electrolytes and electrochromic thin films. A good understanding of the reactive sputtering process is essential when tailoring the thin film properties. This reasoning formed also the guideline for the table of content which mimics a virtual journey from target towards substrate.

Together with the authors, we hope that the different topics discussed in the book will help the novice and experienced scientist to solve some of the problems encountered during the use of this interesting deposition technique.

Gent, January 2008

Diederik Depla
Stijn Mahieu
www.draft.ugent.be

Contents

1 Simulation of the Sputtering Process
T. Ono, T. Kenmotsu, and T. Muramoto 1
1.1 Introduction 1
1.2 Computer Simulation Codes 2
1.3 Total Sputtering Yield 5
1.3.1 Incident-Energy Dependence of Sputtering Yield 5
1.3.2 Incident-Angle Dependence of Sputtering Yield 9
1.4 Differential Sputtering Yield 16
1.4.1 Energy Spectrum of Sputtered Atoms 16
1.4.2 Angular Distribution of Sputtered Atoms 21
1.5 Sputtering from Rough Surface 28
1.6 Sputtering of Compound Targets 30
1.7 Conclusion 37
References 39

2 Electron Emission from Surfaces Induced by Slow Ions and Atoms
R.A. Baragiola and P. Riccardi 43
2.1 Introduction 43
2.2 Physical Mechanisms 44
2.2.1 Excitation Mechanisms 44
2.2.2 Separation of PEE and KEE 46
2.2.3 Electron Transport and Escape into Vacuum 46
2.3 Electron Yields 46
2.3.1 Dependence of the Electron Yields on Ion Velocity 47
2.3.2 Electron Energy and Angular Distributions 48
2.3.3 Electron Emission from Contaminant Surface Layers 48
2.4 The Role of Ion-Induced Electron Emission in Glow Discharges . . . 50
2.4.1 Effect of Electron Recapture at the Cathode 53
2.4.2 Effect of Changes in the Chemical Composition of the Cathode 56

2.5 Outlook . . . 58
References . . . 58

3 Modeling of the Magnetron Discharge
A. Bogaerts, I. Kolev, and G. Buyle . . . 61
3.1 Introduction . . . 61
3.1.1 The Magnetic Field . . . 62
3.1.2 The Magnetron Discharge . . . 63
3.1.3 The Particle–Target Interaction . . . 63
3.1.4 Particle Transport in the Gas Phase . . . 64
3.1.5 Film Growth on the Substrate . . . 64
3.2 Overview of Different Modeling Approaches for Magnetron Discharges . . . 65
3.2.1 Analytical Models . . . 66
3.2.2 Fluid Models . . . 67
3.2.3 The Boltzmann Equation . . . 68
3.2.4 Monte Carlo Simulations . . . 69
3.2.5 Hybrid Models . . . 71
3.2.6 PIC-MCC Simulations . . . 72
3.3 Challenges Related to Magnetron Modeling . . . 74
3.3.1 Secondary Electron Emission Yield (γ) . . . 75
3.3.2 Recapture . . . 75
3.3.3 Electron Mobility . . . 76
3.3.4 Modeling "Industrially Relevant" Magnetron Discharges . . . 76
3.4 Two-Dimensional Semi-Analytical Model for a DC Planar Magnetron Discharge . . . 78
3.4.1 Description of the Model . . . 79
3.4.2 Examples of Calculation Results . . . 81
3.5 PIC-MCC Model for a DC Planar Magnetron Discharge . . . 83
3.5.1 Particle-In-Cell Model . . . 83
3.5.2 Monte Carlo Collision Method . . . 95
3.5.3 Methods for Speeding Up the Calculations . . . 99
3.5.4 Examples of Calculation Results . . . 103
3.6 Extension of the PIC-MCC Model: To Include Sputtering and Gas Heating . . . 115
3.6.1 Description of the Model . . . 116
3.6.2 Examples of Calculation Results . . . 119
3.7 Conclusions and Outlook for Future Work . . . 123
References . . . 124

4 Modelling of Reactive Sputtering Processes
S. Berg, T. Nyberg, and T. Kubart . . . 131
4.1 Introduction . . . 131
4.2 Basic Model for the Reactive Sputtering Process . . . 133
4.3 Steady State Equations . . . 136

4.4 Influence of Material Properties and Processing Conditions 141
4.4.1 Reactivity 141
4.4.2 Sputtering Yield 141
4.4.3 Pumping Speed 142
4.4.4 Target Size 143
4.4.5 Mixed Targets 143
4.4.6 Two Reactive Gases 145
4.4.7 Reactive Co-Sputtering 147
4.4.8 Comment on Pulsed DC Reactive Sputtering 150
4.4.9 Secondary Electron Emission 150
4.4.10 Ion Implantation 150
4.5 Concluding Remarks 151
References 151

5 Depositing Aluminium Oxide:
A Case Study of Reactive Magnetron Sputtering
D. Depla, S. Mahieu, and R. De Gryse 153
5.1 Introduction 153
5.2 Some Experiments 154
5.2.1 A First Series of Experiments 154
5.2.2 A Second Series of Experiments: Oxygen Exposure
and Plasma Oxidation 156
5.2.3 Stability Experiments 164
5.2.4 First Conclusions Based on the Experiments 166
5.3 An Extended Model for Reactive Magnetron Sputtering 167
5.3.1 The Description of Reactive Ion Implantation
During Sputtering 167
5.3.2 The Influence of Chemisorption and Knock-On Effects 171
5.3.3 Calculation of the Reactive Gas Partial Pressure
as a Function of the Reactive Gas Flow 173
5.4 Confrontation Between Experiment and Model 175
5.4.1 Simultaneous Reactive Ion Implantation
and Sputtering Without Chemical Reaction 175
5.4.2 Simultaneous Reactive Ion Implantation
and Sputtering with Chemical Reaction 176
5.5 Towards a More Complete Model
for Reactive Magnetron Sputtering 186
5.5.1 Plasma-Related Topics 186
5.5.2 Deposition Profiles and Erosion Profiles 187
5.5.3 Rotating Magnetrons 191
5.6 Conclusion 193
References 196

6 Transport of Sputtered Particles Through the Gas Phase
S. Mahieu, K. Van Aeken, and D. Depla . . . 199
6.1 Introduction . . . 199
6.2 Radial Distribution Where Sputtered Particles Leave the Target . . . 200
6.3 Energy and Angular Distribution of Sputtered Particles Leaving the Target . . . 201
6.3.1 Sigmund–Thompson Theory for the Linear Cascade Regime . . . 201
6.3.2 Other Analytical Models . . . 204
6.3.3 Comparison to Experimental Results . . . 206
6.3.4 Numerical Method . . . 207
6.3.5 Conclusions . . . 208
6.4 Describing the Collision with the Gas Particle . . . 208
6.4.1 The Mean Free Path . . . 210
6.4.2 The Scattering Angle . . . 211
6.4.3 The Interaction Potential . . . 213
6.5 Gas Rarefaction . . . 217
6.6 Typical Results of a Binary Collision Monte Carlo Code . . . 218
6.7 Specific Example: In-Plane Alignment of Biaxially Aligned Thin Films . . . 223
6.8 Conclusions . . . 224
References . . . 225

7 Energy Deposition at the Substrate in a Magnetron Sputtering System
S.D. Ekpe and S.K. Dew . . . 229
7.1 Introduction . . . 229
7.2 Energy Measurement . . . 231
7.3 Factors Affecting Energy Flux . . . 232
7.3.1 Magnetron Power and Pressure . . . 235
7.3.2 Substrate-Target Distance . . . 235
7.3.3 Electrical Effects . . . 236
7.4 Total Energy per Deposited Atom . . . 237
7.5 Energy Model . . . 239
7.5.1 Sputtered Particles . . . 240
7.5.2 Reflected Neutrals . . . 241
7.5.3 Plasma Radiation . . . 242
7.5.4 Charge Carriers . . . 243
7.5.5 Thermal Radiation . . . 244
7.5.6 Model Results . . . 246
7.6 Conclusions . . . 251
References . . . 251

8 Process Diagnostics
J.W. Bradley and T. Welzel . . . 255
8.1 Introduction . . . 255
8.2 Electrical Probes . . . 256
8.2.1 Probe Techniques . . . 257
8.2.2 Use of Electrical Probes in Pulsed Reactive Sputtering . . . 258
8.3 Mass Spectrometry . . . 270
8.3.1 Mass Spectrometry Technique . . . 270
8.3.2 Application of Mass Spectrometry to Reactive Sputtering . . 271
8.4 Optical Emission Spectroscopy . . . 286
8.4.1 Technique . . . 286
8.4.2 Plasma Emission Monitoring . . . 287
8.4.3 Time-Resolved OES in Pulsed Reactive Sputtering . . . 288
8.5 Optical Imaging . . . 292
8.6 Laser-Induced Fluorescence . . . 293
8.7 Summary . . . 296
References . . . 296

9 Optical Plasma Diagnostics During Reactive Magnetron Sputtering
S. Konstantinidis, F. Gaboriau, M. Gaillard, M. Hecq, and A. Ricard . . . 301
9.1 Introduction . . . 301
9.2 Emission Spectroscopy of Magnetron Plasmas . . . 302
9.3 Resonant Absorption Spectroscopy of Magnetron Plasmas . . . 311
9.4 Laser Spectroscopy of Magnetron Plasmas . . . 320
9.4.1 Previous Works . . . 320
9.4.2 Principle and Achievements . . . 322
9.4.3 Application to Magnetron Discharges . . . 326
9.5 Optical Diagnostic of High-Power Impulse Magnetron Sputtering Discharges . . . 327
9.6 Conclusion . . . 332
References . . . 333

10 Reactive Magnetron Sputtering of Indium Tin Oxide Thin Films: The Cross-Corner and Cross-Magnetron Effect
H. Kupfer and F. Richter . . . 337
10.1 Introduction . . . 337
10.2 The CCE and CME as an Inhomogeneous Target Erosion . . . 338
10.3 Evidence of the CCE and CME From In Situ Measurements . . . 346
10.3.1 Introduction . . . 346
10.3.2 The CCE and the Plasma Properties of Unipolar-Pulsed Single Magnetron Discharges . . . 349
10.3.3 The CME and the Plasma Properties of Bipolar-Pulsed Dual Magnetron Discharges . . . 350
10.3.4 The CME and the Thermal Load of the Substrates . . . 353

10.4 CCE, CME and Film Property Distribution: ITO as an Example . . 354
10.4.1 Introduction . . . 354
10.4.2 Unipolar DC-Pulsed Single Magnetron: CCE and ITO Film Properties . . . 356
10.4.3 Bipolar-Pulsed Dual Magnetron: CME and ITO Film Properties . . . 358
10.5 CCE, CME and the Role of the Atomic Oxygen in the Process Gas . . . 360
References . . . 365

11 Reactively Sputter-Deposited Solid Electrolytes and Their Applications
P. Briois, F. Lapostolle, and A. Billard . . . 367
11.1 Introduction . . . 367
11.2 Crystallographic Basis of the Solid Electrolyte . . . 369
11.2.1 O^{2-} Carriers . . . 369
11.2.2 H^+ Carriers . . . 374
11.2.3 Na^+ Carriers . . . 375
11.2.4 Li^+ Carriers . . . 377
11.2.5 Mixed Conductors . . . 377
11.3 Application of Solid Electrolytes . . . 377
11.3.1 Solid Oxide Fuel Cells . . . 377
11.3.2 Microbatteries . . . 392
11.3.3 Smart Windows . . . 399
11.4 Conclusion . . . 402
References . . . 404

12 Reactive Sputtered Wide-Bandgap p-Type Semiconducting Spinel AB_2O_4 and Delafossite ABO_2 Thin Films for "Transparent Electronics"
A.N. Banerjee and K.K. Chattopadhyay . . . 413
12.1 Introduction . . . 413
12.2 Spinel and Delafossite Material . . . 414
12.2.1 Spinel Materials . . . 414
12.2.2 Delafossite Materials . . . 416
12.3 p-Type Transparent Conducting Oxides Based on Spinel and Delafossite Structure . . . 417
12.3.1 Introduction to Transparent Conducting Oxides . . . 417
12.3.2 Transparent Electronics . . . 418
12.3.3 p-TCO with Spinel Structure . . . 420
12.3.4 p-TCO with Delafossite Structure . . . 422
12.3.5 Other Deposition Techniques: PLD, RF Sputter Deposition, Magnetron Sputtering with RTA, and Ion Exchange Method . . . 425
12.3.6 Reactive Sputtered p-TCO . . . 432

12.4 Transparent Junctions Based on Spinel and Delafossite Oxides 441
12.5 Origin of p-Type Conductivity in Wide-Bandgap Spinel and Delafossite Oxide Materials 448
12.6 Reactive DC Sputter Deposition of Delafossite p-$CuAlO_{2+x}$ Thin Film 455
12.6.1 Introduction 455
12.6.2 Synthesis 457
12.6.3 Results and Discussion 458
12.7 Conclusions and Future Directions 473
12.7.1 Conclusions 473
12.7.2 Future Directions 474
References 477

13 Oxide-Based Electrochromic Materials and Devices Prepared by Magnetron Sputtering
C.G. Granqvist 485
13.1 Introduction 485
13.2 Energy Efficiency of Chromogenic Building Skins 486
13.3 Electrochromic Device Design and Materials 487
13.4 Properties and Applications of Electrochromic Foil 490
13.5 Conclusion and Outlook 493
References 494

14 Atomic Assembly of Magnetoresistive Multilayers
H. Wadley, X. Zhou, and W.H. Butler 497
14.1 Introduction 497
14.1.1 Giant Magnetoresistance 498
14.1.2 Atomic Scale Structure Effects 501
14.1.3 Deposition and Growth Processes 504
14.2 Atomistic Simulations 505
14.2.1 Interatomic Potentials 505
14.2.2 MD Model 515
14.3 Growth of Metal Multilayers 517
14.4 Ion-Assisted Growth of Metal Multilayers 532
14.5 Dielectric Layer Deposition 545
14.6 Ion-Assisted Reactive Growth of Dielectric Layers 553
14.7 Conclusions 555
References 555

Index 561

Contributors

Arghya N. Banerjee
Nevada Nanotechnology Center
Department Electrical Engineering
and Computer Science
University Nevada
Las Vegas, NV 89154, USA
banerjee_arghya@hotmail.com

Raúl A. Baragiola
Laboratory for Atomic
and Surface Physics
University of Virginia
Engineering Physics
Charlottesville, VA 22904, USA
raul@virginia.edu

Sören Berg
The Ångström Laboratory
Uppsala University
Box 534
751 21 Uppsala, Sweden
Soren.Berg@angstrom.uu.se

Alain Billard
Laboratoire d'Etudes et de recherches
sur les Matériaux
les Procédés et les Surfaces
(LERPMS-UTBM)
Site de Montbéliard
90010 Belfort cedex, France
alain.billard@utbm.fr

Annemie Bogaerts
Research Group PLASMANT
Department of Chemistry
University of Antwerp
Universiteitsplein 1
2610 Wilrijk-Antwerp, Belgium
Annemie.Bogaerts@ua.ac.be

James W. Bradley
Department of Electrical Engineering
and Electronics
The University of Liverpool
Brownlow Hill
Liverpool L69 3GJ, UK
j.w.bradley@liverpool.ac.uk

Pascal Briois
Laboratoire d'Etudes et de recherches
sur les Matériaux
les Procédés et les Surfaces
(LERPMS-UTBM)
Site de Montbéliard
90010 Belfort cedex, France
pascal.briois@utbm.fr

William H. Butler
Department of Physics
and Astronomy
University of Alabama
Tuscaloosa, Alabama, USA
wbutler@mint.ua.edu

Guy Buyle
Department of Solid State Sciences
Gent University
Krijgslaan 281/S1
9000 Gent, Belgium
Guy.Buyle@centexbel.be

Kalyan K. Chattopadhyay
Thin Film
and Nanoscience Laboratory
Department of Physics
Jadavpur University
Jadavpur, Kolkata 700032, India
kalyan_chattopadhyay@yahoo.com

Roger De Gryse
Gent University
Department of Solid State Sciences
Krijgslaan 281 (S1)
9000 Gent, Belgium
Roger.Degryse@ugent.be

Diederik Depla
Gent University
Department of Solid State Sciences
Krijgslaan 281 (S1)
9000 Gent, Belgium
Diederik.Depla@ugent.be

Steven K. Dew
Department of Electrical
and Computer Engineering
University of Alberta
Edmonton, Alberta
T6G 2V4, Canada
steven.dew@ualberta.ca

Samuel D. Ekpe
Department of Electrical
and Computer Engineering
University of Alberta
Edmonton, Alberta
T6G 2V4, Canada
ekpe@ece.ualberta.ca

F. Gaboriau
Laplace, University of Paul Sabatier
118 route de Narbonne
31062 Toulouse, France
gaboriau@cpat.ups-tlse.fr

M. Gaillard
CAPST, SungKyunKwan University
300 Chun-Chun-Dong
Jangan-gu, Suwon 440-746, Korea
mireille.gaillard@ua.ac.be

C.G. Granqvist
Department of Engineering Sciences
The Ångström Laboratory
Uppsala University
Box 534
75121 Uppsala, Sweden
Claes-Goran.Granqvist@
Angstrom.uu.se

M. Hecq
Laboratoire de Chimie Inorganique
et Analytique
Université de Mons-Hainaut
Avenue Copernic 1
7000 Mons, Belgium
Michel.Hecq@umh.ac.be

Takahiro Kenmotsu
Department of Environmental Risk
Management
Kibi International University
8 Iga-cho, Takahashi-shi
Okayama 716-8508, Japan
kenmotsu@kiui.ac.jp

Ivan Kolev
Research Group PLASMANT
Department of Chemistry
University of Antwerp
Universiteitsplein 1
2610 Wilrijk-Antwerp, Belgium
Ivan.Kolev@ua.ac.be

Stephanos Konstantinidis
Laboratoire de Chimie Inorganique et Analytique
Université de Mons-Hainaut
Avenue Copernic 1
7000 Mons, Belgium
Stephanos.Konstantinidis@umh.ac.be

Tomas Kubart
The Ångström Laboratory
Uppsala University
Box 534
751 21 Uppsala, Sweden
Tomas.Kubart@angstrom.uu.se

H. Kupfer
University of Technology Chemnitz
Institute of Physics
09107 Chemnitz, Germany
h.kupfer@physik.tu-chemnitz.de

Frédéric Lapostolle
Laboratoire d'Etudes et de recherches sur les Matériaux
les Procédés et les Surfaces (LERPMS-UTBM)
Site de Montbéliard
90010 Belfort cedex, France
Frederic.Lapostolle@utbm.fr

Stijn Mahieu
Department of Solid State Sciences
Gent University
Krijgslaan 281 (S1)
9000 Gent, Belgium
Stijn.Mahieu@ugent.be

Tetsuya Muramoto
Department of Computer Simulation
Okayama University of Science
1-1 Ridai-cho, Okayama
700-0005, Japan
muramoto@sp.ous.ac.jp

Tomas Nyberg
The Ångström Laboratory
Uppsala University
Box 534
751 21 Uppsala, Sweden
Tomas.Nyberg@angstrom.uu.se

Tadayoshi Ono
Department of Computer Simulation
Okayama University of Science
1-1 Ridai-cho, Okayama
700-0005, Japan
ono@sp.ous.ac.jp

A. Ricard
Laplace, University of Paul Sabatier
118 route de Narbonne
31062 Toulouse, France
ricard@cpat.ups-tlse.fr

Pierfrancesco Riccardi
Laboratorio IIS
INFN gruppo collegato di Cosenza
Dipartimento di Fisica
Università della Calabria
87036 Arcavacata di Rende (CS)
Italy
riccardi@fis.unical.it

F. Richter
University of Technology Chemnitz
Institute of Physics
09107 Chemnitz, Germany
f.richter@physik.tu-chemnitz.de

Koen Van Aeken
Department of Solid State Sciences
Ghent University
Krijgslaan 281/S1
9000 Ghent, Belgium
Koen.VanAeken@ugent.be

Haydn Wadley
Department of Materials Science and Engineering
University of Virginia
Charlottesville, Virginia, USA
hnw4z@virginia.edu

Thomas Welzel
Chemnitz University of Technology
Institute of Physics
09107 Chemnitz, Germany
t.welzel@physik.tu-chemnitz.de

Xiaowang Zhou
Department of Mechanics
of Materials
Sandia National Laboratories
Livermore, California, USA
xzhou@sandia.gov

1

Simulation of the Sputtering Process

T. Ono, T. Kenmotsu, and T. Muramoto

1.1 Introduction

In this chapter, we deal with *sputtering* of target materials bombarded with energetic particles. In this process, target atoms are removed from the surface by collisions between a projectile and/or recoil atoms produced and the atoms in the near-surface layers of the target material.

Sputtering is utilized widely and positively as a useful technique to produce thin films, to make trace impurity analyses of materials of all sorts (e.g., Secondary Ion Mass Spectroscopy), for surface treatment and surface processing, and also for a variety of many other technological applications. However, sputtering plays an undesired role in some cases, on the other hand. The first wall and the divertor of a thermonuclear fusion device, for example, are eroded mainly by impinging plasma ions, which causes the core plasma to be contaminated if sputtered atoms enter it, resulting in insufficient heating of fuel. Therefore, quantitative knowledge on sputtering is required to be determined accurately and compiled for these scientific researches or technological development. Computer simulations of sputtering have contributed greatly to such purposes and to elucidate the pertinent processes. In what follows, we give a quantitative account of and highlight the results obtained mainly by us from computer simulations of sputtering.

In Sect. 1.2 we introduce our computer codes (Monte Carlo (MC) binary code, dynamical Monte Carlo code, and molecular dynamics (MD) code) used for sputtering calculations and the outlines of the codes necessary to discuss the results are described.

Section 1.3 is concerned with incident-energy dependence and angular dependence of total sputtering yield. The sputtering mechanisms of a target material bombarded with heavy and light ions are outlined. Then, semi-empirical formulae for energy dependence are compared with experimental and calculated data. The sputtering mechanism for light-ion bombardment from oblique incidence is mentioned in terms of the knockout process. New semi-empirical formulae to reproduce experimental and calculated data of

incident-angle dependence of total sputtering yield are introduced. We also present incident-angle dependence of tungsten self-sputtering yield calculated with our computer codes for very low incident energy. The large difference found at glancing angles of incidence between the MC and the MD data is accounted for using the contour maps of deposited energy density on the surface calculated in these simulations. Section 1.4 describes differential sputtering yields with respect to energy and ejection angle of sputtered atoms. In particular, we indicate that the energy spectrum of sputtered atoms from heavy target materials with low-energy light ions can be reproduced well by semi-empirical formulae proposed recently by us. The energy spectra of sputtered atoms calculated with the MC and the MD codes are compared with each other. The components of sputtered atoms with very low energy obtained with the MD are discussed. We present typical angular distributions of sputtered atoms obtained with experiments and calculations. The difference in the angular distributions for heavy- and light-ion irradiation is described. A new semi-empirical formula that can reproduce even the heart-shaped distribution corresponding to heavy- and moderately heavy ions with very low-energy bombardment is presented.

In Sect. 1.5, we mention the effect of surface roughness on sputtering with low- and high-energy ions. Low-energy ions incident on a rough surface is equivalent to randomizing incident angle, and sputtering with high-energy ions is affected by the averaged low-density of a rough surface.

Section 1.6 goes into sputtering of compound materials. Sputtering of multicomponent targets is complex compared with that of monoatomic targets. In sputtering of multicomponent targets, compositional change near a surface is unavoidable under ion bombardment and depends on target systems. Kinetic and thermal processes occurring in a material result in the compositional change. Ion-fluence dependence of the compositional change for a Cu–Ni alloy was calculated with the dynamic Monte Carlo simulation code which includes both kinetic and thermal processes.

1.2 Computer Simulation Codes

Comprehensive reviews on computer simulation codes used widely for sputtering have been done [1–4]. According to how atomic collisions occurring in a solid are modeled, these codes are classified basically into two groups, i.e., MC codes which treat atomic collisions with a MC method in a binary collision approximation (BCA), and classical MD codes which assume that incident projectiles collide with a system of many atoms involved and solve time evolutionally the classical dynamics of the system from knowledge of the interaction forces between particles. Generally, MC codes are suited for simulations in much larger space- and timescales than MD ones. However, as incident energy of ions reaches a low-energy range, e.g., around 100 eV,

the effective interactive region that a moving atom feels widens. Accordingly, BCA breaks down, and MD is required, instead.

Since ACAT [5] code, ACAT-DIFFUSE [6] code, DYACAT [7], and a MD code [8] have been described in detail, we describe here only the main features of these codes necessary to discuss the results obtained with these codes.

The ACAT and the TRIM.SP [2, 9] codes are of the MC type. While the TRIM.SP code pursues atomic collisions by using a mean free path like many other MC codes, the ACAT code assumes an amorphous target by employing the so-called "cell model," i.e., an amorphous target is composed of simple cubic cells, in each of which the site of a target atom is chosen stochastically with a lattice constant $\lambda = \Omega^{1/3}$, where the atomic volume $\Omega = 1/N$, N the number density of the target material, and the surface is atomically rough in scale of $\lambda/2$. Moreover, one can prepare desired surface roughness by adding more cells on the original surface, as indicated in Fig. 1.1.

The DYACAT code is a dynamical version of the ACAT code. In this code, the binary collision events are arranged in order of time they occur. The code can consider collisions between two moving atoms as well as a non-Markov process, which is very important for polyatomic ion bombardment on a solid. The non-Markov process is a random process whose future probabilities are determined by its most recent and all the past values. In the code, the process corresponds with collisions between a moving atom and point defects produced from a simultaneously ongoing collision cascade. Since distant collisions become important in a low-energy range as mentioned above, the code considers many-body collisions among a moving atom and several target atoms located in an effective interaction range by a limited-MD calculation. Therefore, the DYACAT code can be regarded as a MD code-like unique BCA code.

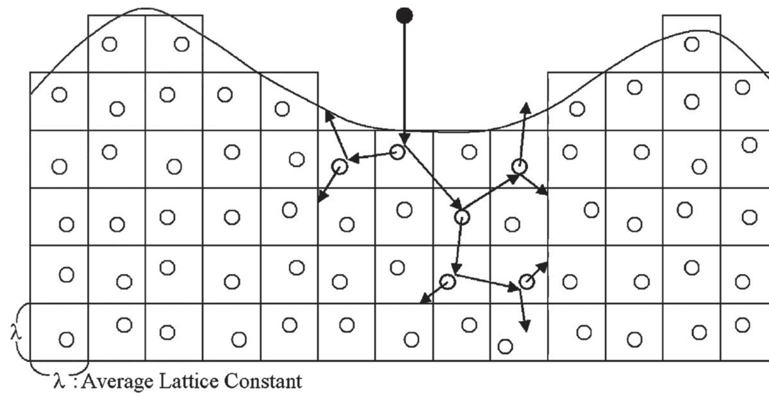

Fig. 1.1. Cell model of a rough surface employed in the ACAT code. *Open circles* stand for atoms located randomly in cubic cells

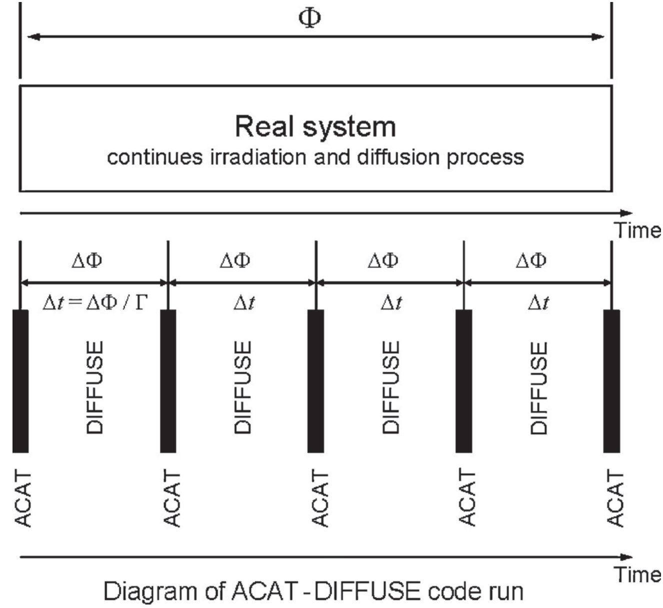

Fig. 1.2. Schematic diagram of the work flow of the ACAT-DIFFUSE routines

The ACAT-DIFFUSE code can calculate sputtering of an amorphous monoatomic and composite materials being irradiated by ions. The code is based on the ACAT code and the DIFFUSE [10] code and its basic concept is schematically shown in Fig. 1.2. The ACAT part of the code calculates the slowing-down processes of implanted projectiles and recoil atoms produced, together with the associated vacancy and range distributions. A large total dose Φ is divided into smaller dose increment $\Delta\Phi$ during which the target composition is not varied appreciably by incident ions. The bunch of ions corresponding to $\Delta\Phi$ is assumed to hit the target material simultaneously and to be slowed down instantaneously. Slowdown of ions, together with the associated vacancies and range distributions are calculated in the ACAT part. Mobile atoms, not trapped in trapping sites, diffuse during the time interval of $\Delta\Phi/J$ (J being the ion flux). The DIFFUSE part copes with the thermal processes of preimplanted and currently implanted ions and recoil atoms produced by solving the diffusion equations numerically. The two routines are iteratively repeated n times, where $n = \Phi/\Delta\Phi$.

As mentioned above, MD determines the dynamics of a system of many atoms by solving Newton's laws of motion for each particle of the system. A well-known numerical calculation method is Verlet algorithm [11]. The most important factor in MD calculations is atomic interaction force. For a few-body system, the force can be calculated by quantum dynamics. However, for a large-scale system, the force is described by semi-empirical many-body potentials in view of calculation speed. If a constrained MD simulation on

temperature is required, the Langevin MD (LMD) method [12] may be employed to combine the system with an external heat bath. In sputtering MD simulations, since one can prepare only a finite target, energy dissipation to the external heat bath has to be considered using a LMD method.

A large number of computer codes have been developed in the fields of ion-implantation and ion-surface interactions, as discussed partly in this chapter. For convenience, those codes widely used are categorized as to atomic process and type of atomic collisions occurring in solids they employ, as depicted in Table 1.1.

1.3 Total Sputtering Yield

1.3.1 Incident-Energy Dependence of Sputtering Yield

A measure of the erosion due to ion irradiation is *sputtering yield*, which is defined as a ratio of the number of sputtered atoms to the number of incident projectiles. A large amount of experimental and calculated data on incident-energy dependence of sputtering yield of monoatomic and multicomponent solids for normal incidence have been produced and accumulated [13–19].

The sputtering mechanism can be classified into two categories as schematically indicated in Fig. 1.3. When relatively heavy ions hit a solid surface, they deposit their energy near the surface and a collision cascade develops, resulting in the ejection of target atoms from the surface (mechanism I) [20]. On the other hand, incoming light ions such as H^+ and D^+ can not produce a collision cascade near the surface because the energy they transfer to target atoms in collisions is not enough to generate a collision cascade. Instead, those ions are reflected from inside the target material and hit near-surface atoms, causing those recoil atoms to leave from the surface if they receive sufficient energy to overcome the surface barrier (mechanism II) [21–23]. As the mass of incident ions becomes lighter, the sputtering mechanism shifts gradually from mechanisms I to II. For ions with intermediate mass, such as Ar^+, both mechanisms I and II contribute to the actual total sputtering yield.

Considering the above sputtering mechanism, Yamamura et al. [17] revised their old semi-empirical formulae [24, 25] by interpolating them to propose a new one (hereafter called *Yamamura formula*) for the energy dependence of sputtering yield $Y(E)$ of monoatomic solids for normal incidence of projectiles, as given by

$$Y(E) = 0.042\frac{Q(Z_2)\alpha^*(M_2/M_1)}{U_\mathrm{s}}\frac{S_\mathrm{n}(E)}{1+\Gamma k\varepsilon^{0.3}}\left[1-\sqrt{\frac{E_\mathrm{th}}{E}}\right]^s, \tag{1.1}$$

where E is projectile energy and M_1, M_2 are the masses of a projectile and a target atom in a.m.u., respectively, and the numerical factor in units of $\mathrm{\AA}^{-2}$. The factor Γ has the form

Table 1.1. Computer codes used in the fields of ion-implantation and ion-surface interactions

Slowing Down Process						Thermal Process
Binary Collision Approximation				Molecular Dynamics		Local Mixing Model
Simple MC		Dynamical MC				
ACAT[1]	ACOCT[5]	TRIDYN[10]	EVOLVE[12]	MDACOCT[24]	MD-TOPS[26]	DIFFUSE[16]
TRIM[2]	MARLOWE[6]	T-DYN[11]	dynamic-SASAMAL[13]	PARASOL[25]	SPUT2SI[29]	PIDAT[17]
TRIM.SP[3]	Crystal-TRIM[7]			MODYSEM[27]	SPUT3[28]	
SASAMAL[4]	COSIPO[8]			MOLDYCASK[30]	QDYN[32]	
	IMSIL[9]			MOLDY[31]	REED[33]	
		DYACAT[14] DYACOCT[15]				
		ACAT-DIFFUSE[19] ACAT-DIFFUSE-GAS[20] EDDY[23] TMAP4[18] TRIDYN+PIDAT[21] TRIDYN+DIFFUSEDC+YCEHM[22]				

(1) Y. Yamamura and Y. Mizuno, Research report of Institute of Plasma Physics, Nagoya University IPPJ-AM-40 (1985).
(2) J.P. Biersack and L.G. Haggmark, Nucl. Instr. Meth. 174 (1980) 257.
(3) J.P. Biersack and W. Eckstein, Appl. Phy. A34 (1984) 73.
(4) Y. Miyagawa and S. Miyagawa, J. Appl. Phys. 54 (1983) 7124.
(5) Y. Yamamura and W. Takeuchi, Nucl. Instrum. Methods B29 (1987) 461.
(6) M.T. Robinson and I.M. Torrens, Phys. Rev. B9 (1974) 5008.
(7) M. Posselt, Radiat. Eff. Def. Solid. 130/131 (1994) 87.
(8) M. Hautala, Phys. Rev. B30 (1984) 5010.
(9) G. Hobler, H. Potzl, L. Gong and H. Ryssel, in: Simulation of Semicondoctor Devices and Process, eds. W. Fichtner and D. Aemmer, Vol. 4 (Hartung-Gorre, Konstanz, 1991) p.389.
(10) W. Möller and W. Eckstein, Nucl. Instr. Meth. B 2 (1984) 814.
(11) J.P. Biersack, S. Berg and C. Nender, Nucl. Instr. Meth. B59–60 (1991) 21.
(12) M.L. Roush, T.S. Andreadis and O.F. Goktepe, Radiat. Eff. 55 (1981) 119.
(13) Y. Miyagawa, M. Ikeyama, K. Saitoh, G. Massouras, S. Miyagawa, J. Appl. Phys. 70 (1991) 7289.
(14) Y. Yamamura, Nucl. Instrum. Methods B33 (1988) 493.
(15) Y. Yamamura, I. Yamada and T. Takagi, Nucl. Instr. Meth. B37–38 (1989) 902.
(16) K.L. Wilson and M.I. Baskes, J. Nucl. Mater. 76/77 (1978) 291.
(17) W. Möller, Max-Plank-Institute für Plasmaphysik, Report IPP 9/44 (1983).
(18) G.R. Longhurst, D.F. Holland, J.L. Jones, B.J. Merrill, TMAP4 User's Manual, EGG-FS-10315, Idaho National Engineering and Environmental Laboratory, 1992.
(19) Y. Yamamura, Nucl. Instr. Meth. B 28 (1987) 17.
(20) M. Ishida, Y. Yamaguchi and Y. Yamamura, Thin Solid Films 334 (1998) 225.
(21) W. Eckstein, V.I. Shulga, J. Roth, Nucl. Instr. Meth. B 153 (1999) 415.
(22) K. Schmid and J. Roth, J. Nucl. Mater. 313–316 (2003) 302.
(23) K. Ohya and R. Kawakami, Jpn. J. Appl. Phys. 40 (2001) 5424.
(24) K. Yorizane, T. Muramoto and Y. Yamamura, Nucl. Instr. Meth. B153 (1999) 292.
(25) G. Betz, R. Kirchner, W. Husinsky, F. Rudenauer and H.M. Urbassek, Radiation Effects and Defects in Solids 130/131 (1994) 251.
(26) Javier Domínguez-Vázquez, E. Pablo Andribet, A. Mari Carmen Pérez-Martín, José J. Jiménez-Rodríguez, Radiation Effects and Defects in Solids 142 (1997) 115.
(27) V. Konoplev and A. Gras-marti, Philosophical magazine A71 (1995) 1265.
(28) M.H. Shapiro and T.A. Tombrello, Nucl. Instr. Meth. B84 (1994) 453.
(29) M.H. Shapiro, T.A. Tombrello and D.E. Harrison, Jr., Nucl. Instr. Meth. B30 (1988) 152.
(30) T. Diaz de la Rubia and M.W. Guinan, J. Nucl. Mater. 174 (1990) 151.
(31) B.L. Holian, The MOLDY program is filed in mass storage at the Los Alamos National Laboratory (1975).
(32) D.E. Harrison, Jr. and M.M. Jakas, Radiat. Eff. 99 (1986) 153.
(33) Jeong-Won Kang, E.S. Kang, M.S. Son, and H.J. Hwang, Journal of Vacuum Science & Technology B18 (2000) 458–461.

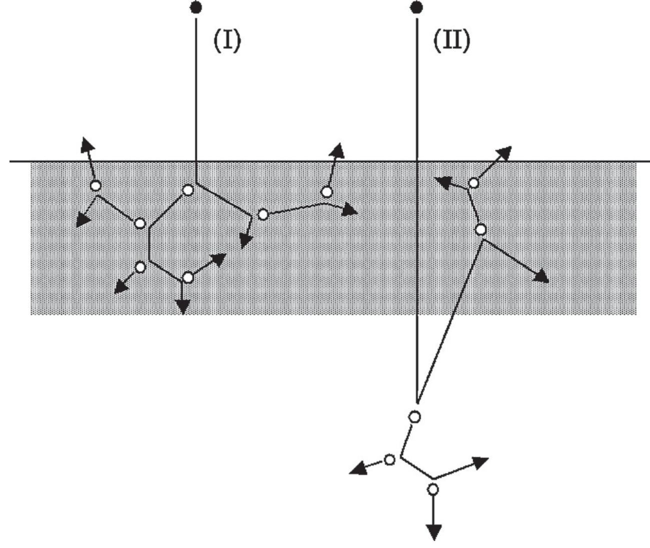

Fig. 1.3. Schematic diagram of the sputtering mechanisms. The case (I) indicates the mechanism for relatively heavy-ion bombardment, and the (II) that for light-ion bombardment

$$\Gamma = \frac{W(Z_2)}{1 + (M_1/7)^3}. \tag{1.2}$$

The surface binding energy of a target material U_s, the best-fit values of the dimensionless parameters $W(Z_2)$, $Q(Z_2)$, and s are tabulated in [17]. The best-fit values of α^* are described as a function of a mass ratio M_2/M_1 in the following manner:

$$\alpha^* = \begin{cases} 0.249(M_2/M_1)^{0.56} + 0.0035(M_2/M_1)^{1.5}, & M_1 \leq M_2, \\ 0.0875(M_2/M_1)^{-0.15} + 0.165(M_2/M_1), & M_1 \geq M_2. \end{cases} \tag{1.3}$$

E_th is sputtering threshold energy and is expressed by the following best-fit functional relation

$$\begin{aligned} \frac{E_\mathrm{th}}{U_\mathrm{s}} &= \frac{6.7}{\gamma}, & M_1 \geq M_2, \\ &= \frac{1 + 5.7(M_1/M_2)}{\gamma}, & M_1 \leq M_2, \end{aligned} \tag{1.4}$$

where γ is energy transfer factor in an elastic collision defined as $\gamma = 4M_1M_2/(M_1 + M_2)^2$. k_e is the Lindhard electronic stopping coefficient [26], and S_n is the nuclear stopping cross section expressed by

$$S_\mathrm{n}(E) = \frac{84.78 Z_1 Z_2}{\left(Z_1^{2/3} + Z_2^{2/3}\right)^{1/2}} \frac{M_1}{M_1 + M_2} s_\mathrm{n}^\mathrm{TF}(\varepsilon), \tag{1.5}$$

in units of eV Å^2 per atom. Note that the numerical factor of 8.478 in (21) in Ref. [17] should be corrected to 84.78 as indicated in (1.5). ε is reduced LSS energy [26], and $s_n^{TF}(\varepsilon)$ is reduced nuclear stopping cross section and is approximated by an analytic fit to the Thomas–Fermi potential [13]. *Yamamura formula* was applied successfully to the cases of multicomponent target materials as described below.

There are other semi-empirical expressions for $Y(E)$, called the "*Bohdansky formula*" [27] and the "*revised Bohdansky formula*", which were used to represent a large number of experimental and calculated data [14, 15, 28].

The discrepancy of the sputtering yields calculated with the TRIM.SP and the ACAT codes is generally small. The above-mentioned *revised Bohdansky* and *Yamamura formulae* can represent experimental results within the errors of better than 30% in many cases, but more than 50% in special cases such as H^+ and D^+ ions onto C for low E in which chemical erosion might take place [14]. The deviations are seen in some cases for incident energies of high keV and in the threshold energy region.

Sputtering yield of Cu target materials by 5 keV Ar^+ impact calculated with the ACAT and the MD codes is tabulated in Table 1.2.

In this MD simulation, the Cu–Cu interactions are described by TB-SMA potential [29] and the Moliere potential [30] for an equilibrium range and a short range, respectively. The Ar–Cu interaction is calculated by the Lennard–Jones [31] and Moliere potentials which are smoothly connected in a similar manner to TB-SMA + Moliere potential. We use a local electronic energy loss model based on the Firsov model [32], which is corrected by the Lindhard–Scharff formula [26]. In a microscopic view, a polycrystalline target looks like a randomly oriented crystal. Therefore, in this MD simulation, we used a random surface model to reproduce the sputtering of a polycrystalline target. In this model, the target crystal is produced by a set of primitive translation vectors, which is oriented randomly for each incidence.

It is shown the current simulations could reproduce almost the experimental sputtering yield [33, 34] of polycrystalline and crystal Cu target materials. The energy dependence of sputtering yield for Ar^+ ions incident on Cu obtained with experiments, MD calculations and *Yamamura formula* (1.1) are illustrated in Fig. 1.4. It is clear from the figure that the simulation results and the formula are in good agreement with the experimental values.

Table 1.2. Calculated and experimental sputtering yield for 5 keV $Ar^+ \rightarrow$ Cu at $\theta = 0°$

	Poly.	(111)
Experiment	5[a]	9[b]
ACAT	5.2	
MD	6.8	9.6

[a] Reference [33]
[b] Reference [34]

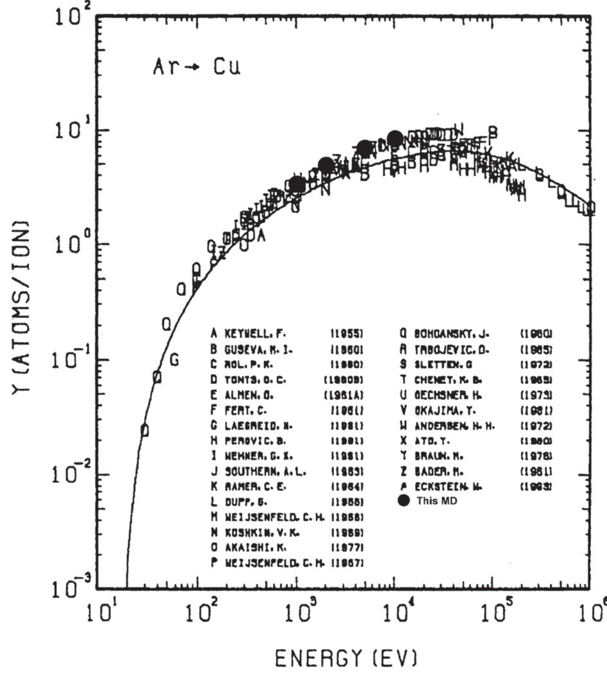

Fig. 1.4. Energy dependence of Ar^{+} ions incident on Cu obtained with experiments, ACAT and MD calculations and *Yamamura formula* (1.1)

Yamamura formula (1.1) can represent sputtering yield data of multicomponent materials by replacing Z_2, M_2, and U_s in (1.1) with their average values such as $\langle Z_2 \rangle = \sum c_i Z_{2,i}$, $\langle M_2 \rangle = \sum c_i M_{2,i}$, and $\langle U_\mathrm{s} \rangle = \sum c_i U_{\mathrm{s},i}$ where c_i is the atomic fraction of ith element [35,36]. For threshold energy, however, the maximum value of $\{E_{\mathrm{th},i}\}$ is chosen except for oxygen ion bombardment for which the threshold energy is a fitting parameter, where $E_{\mathrm{th},i}$ is the threshold energy of the monoatomic solid of ith element for the projectile. The experimental and calculated sputtering yields of oxide targets displayed in Fig. 1.5 are represented well by (1.1) with the above replacements.

1.3.2 Incident-Angle Dependence of Sputtering Yield

A large quantity of experimental and calculated data on incident-angle dependence of sputtering yield of monoatomic and composite solids have been produced and accumulated [14,18,19,37–43].

Generally, while the incident angle, measured from the surface normal, of ions is small, the yield increases with increasing incident angle because of a cascade developed more close to the surface; after passing the maximum, it decreases with increasing incident angle for large incident angles since the screening effect of neighboring surface atoms begins to prevent incident ions

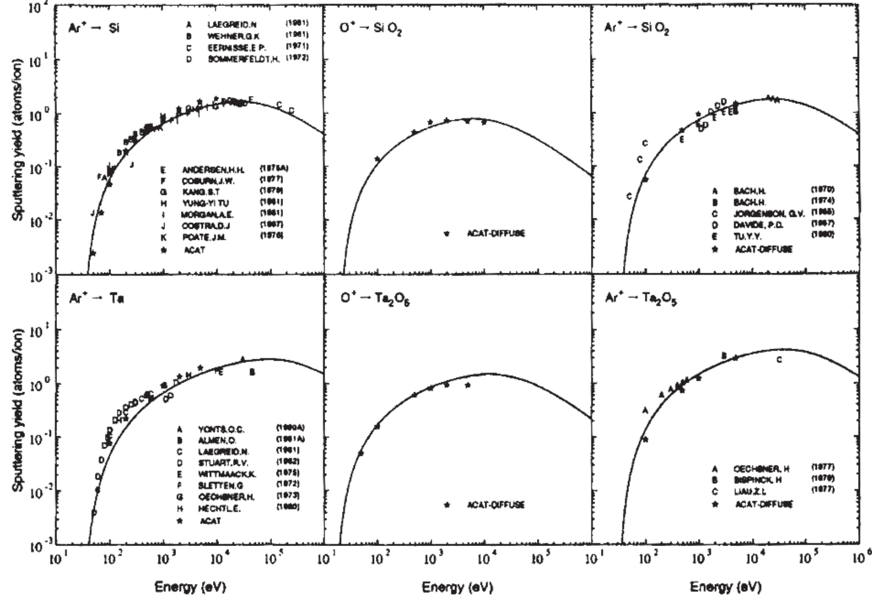

Fig. 1.5. Energy dependence of sputtering yields of Si, Ta, SiO_2, and Ta_2O_5 for argon and oxygen bombardment, where *solid lines* correspond to (1.1), and the experimental data of monoatomic solids are from [17] and those of oxide from [36]

from entering the surface; finally it decreases sharply since incident ions are almost all reflected without giving energy to the solid.

Taking into account the probability that incident ions can enter the surface of a solid to add a corresponding factor to a formula given by Sigmund [20], Yamamura [43] proposed a semi-empirical formula for incident-angle dependence of sputtering yield expressed by

$$\frac{Y(E,\theta)}{Y(E,0)} = X^f \exp[-\Sigma(X-1)], \tag{1.6}$$

where $X = 1/\cos\theta$, and the term X^f was proposed by Sigmund [20]. $Y(E,\theta)$ is sputtering yield for incident angle θ measured from the surface normal. Σ is a physical quantity that is proportional to scattering cross section, and f and Σ are fitting parameters to be determined by adjusting the formula to experimental or calculated data. It was shown that (1.6) can generally reproduce well experimental and calculated data on the incident-angle dependence of sputtering yield with light ions [14, 43]. The validity of (1.6) was checked to indicate that it is acceptable for not-too-low energies, i.e., above 1 keV, though it is not correct for self-sputtering and for heavy projectiles with energies near the threshold energy [28]. However, the second conclusion seems to be not worth special mention, since heavy projectiles with such low energies can not fulfill the necessary condition for developing a genuine collision

cascade near a solid surface that (1.6) assumes as a premise for heavy-ion bombardment [43].

To account for the binding energies of incoming ions, for example, self-bombardment, where large angles of incidence cannot be reached, (1.6) has been improved, resulting in a new formula expressed as

$$Y(E,\theta) = Y(E,0)\left\{\cos\left[\left(\frac{\theta}{\theta_0}\frac{\pi}{2}\right)^c\right]\right\}^{-f} \exp\left\{b\left(1 - 1/\cos\left[\left(\frac{\theta}{\theta_0}\frac{\pi}{2}\right)^c\right]\right)\right\}, \tag{1.7}$$

$$\theta_0 = \pi - \arccos\sqrt{\frac{1}{1+E/E_{\mathrm{sp}}}} \geq \frac{\pi}{2}, \tag{1.8}$$

with the fit parameters $f,\ b,\ c$ [44]. E_{sp}, the binding energy of a projectile, has to be provided. For self-bombardment, it is equal to the surface binding energy of target atoms; for noble gas projectiles $E_{\mathrm{sp}} = 0$; for hydrogen isotopes $E_{\mathrm{sp}} =$ 1 eV is assumed. With the use of large datasets [18], new fits threshold energies for different ion-target combinations and for incident angle at several mass ratios are given [18]. The angular dependence of sputtering yield obtained with the experiment and (1.6) for 1 and 8 keV H^+ incident on Ni is shown in Fig. 1.6a, and that for 30 eV W^+ onto W from (1.6) and (1.7) in Fig. 1.6b [44,45].

Modeling of surfaces is a very important factor for sputtering simulations. For oblique incidence, a collision cascade tends to be developed more closely to the surface. Thus, the surface-model dependence is expected to be clearly shown up for grazing incidence. Hence, we performed simulations of low-energy ion sputtering to examine it.

Again, we make a comparison of incident-angle dependence of sputtering in a low energy range calculated with both ACAT and TRIM.SP codes. Figure 1.7 shows simulation results of the TRIM.SP and the ACAT codes. The TRIM.SP result for grazing incidence approaches a finite yield. To understand this feature, let us mention the surface treatment of the TRIM.SP code. Target atoms are searched in an inner cylinder and coaxial outer ring cylinders with volume Ω and length λ along the pass of a moving atom, where the atomic volume $\Omega = 1/N,\ \lambda = \Omega^{1/3}$ and N is the number density of a target material. The bottom faces of the cylinders are called "target disks." A target atom is set randomly on each target disk. A target atom found outside the surface is disregarded. If several target atoms are found, the one on the inner disk is selected. Thus, the code contains more short-range collisions than the ACAT code.

Open squares in Fig. 1.7 indicate sputtering yield derived with a modified ACAT code that forces the projectiles to collide first in the cell at an origin, and that contains more short-range collisions. For grazing incidence, the TRIM.SP result comes somewhere between the ACAT and the modified

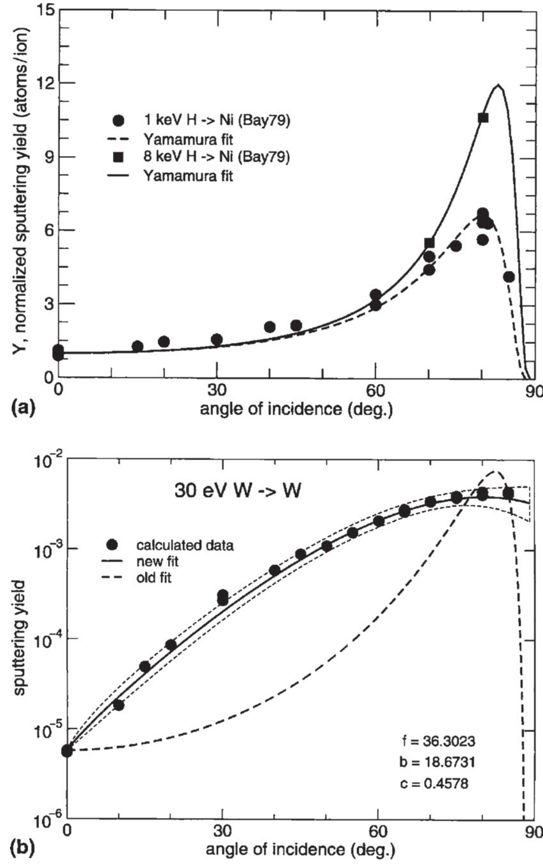

Fig. 1.6. Angular dependence of sputtering yield. (**a**) Obtained with the experiment and (1.6) for 1 and 8 keV H^+ incident on Ni and (**b**) that for 30 eV W^+ onto W from (1.6) and (1.7) [44]

ACAT results. Thus, the large energy deposited by short-range collisions increases sputtering yield in the TRIM.SP case.

The knockout process of a surface target atom executed by an incident light ion becomes dominant at large angles [46, 47]. The knockout process at large angles is divided roughly into *direct* and *indirect* ones, where a "*direct*" one means the *direct* knockoff of a surface atom by an incoming ion and an "*indirect*" one the knockoff of a surface atom by an incident ion which is scattered just before near the surface by the other target atoms, as illustrated in Fig. 1.8. While only the *indirect* one works for the not-too-oblique incidence, the *direct* one plays a major role at grazing angles of incidence. Equation (1.6) does not include the contribution from the *direct* knockout process to the sputtering yield. Later, Yamamura et al. [47] presented a new formula for light ions where that process was also taken into account, as given by

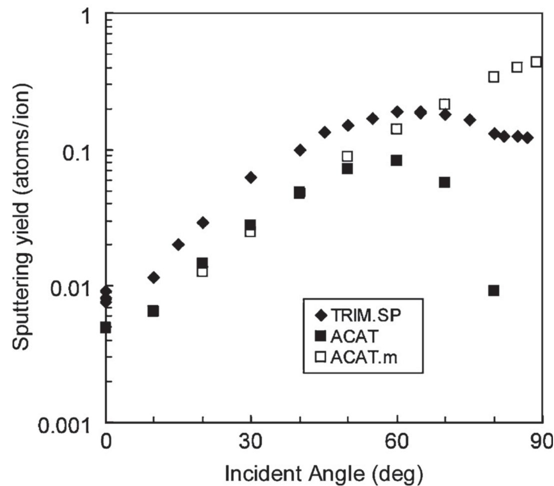

Fig. 1.7. Incident-angle dependence of sputtering yield for 100 eV W → W. *Closed diamonds* are the results of TRIM.SP [2, 9], the *open squares* are the results of the modified ACAT code that contains more short-range collisions

$$\frac{Y(E,\theta)}{Y(E,0)} = T^f \ \exp[-\Sigma(X-1)], \tag{1.9}$$

where $T = (1 + A\sin\theta)/\cos\theta$, $X = 1/\cos\theta$. The term sin θ included in T reflects the contribution of the *direct* knockout process. f, Σ, and A are parameters and estimated by adjusting the formula to experimental or calculated data.

Most recently three parameters were estimated for the ACAT data of D^+ ions incident obliquely on C, Fe, and W materials in the energy ranges from tens eV to 10 keV [48]. Then, the parameters were expressed as a function of incident energy. As displayed in Fig. 1.9, the dependence of normalized physical sputtering yield on incident-angle derived from (1.9) using the functions has been compared with the ACAT data for 200 eV and 1 keV D^+ ions incident obliquely on C and with those from (1.9) with not using the functions and from (1.6). We found that the three formulae all agree well with the ACAT data, except for 20–40% difference between the ACAT data and (1.6) at angles of not-too-oblique incidence for 1 keV ions.

Figure 1.10 indicates incident-angle dependence of tungsten self-sputtering for incident energy of 100 eV, where the solid squares, triangles, and circles represent ACAT, DYACAT, and MD results. The MD simulation assumed a random surface. The yields for normal incidence obtained with the DYACAT and MD codes are almost equal to 0.013 atoms/ion which was derived by extrapolating the experimental database of sputtering in [17] using (1.9). For grazing incidence ($\theta \geq 80°$), the ACAT yield approaches zero since the surface normal component of the incident velocity also becomes close to zero. As a

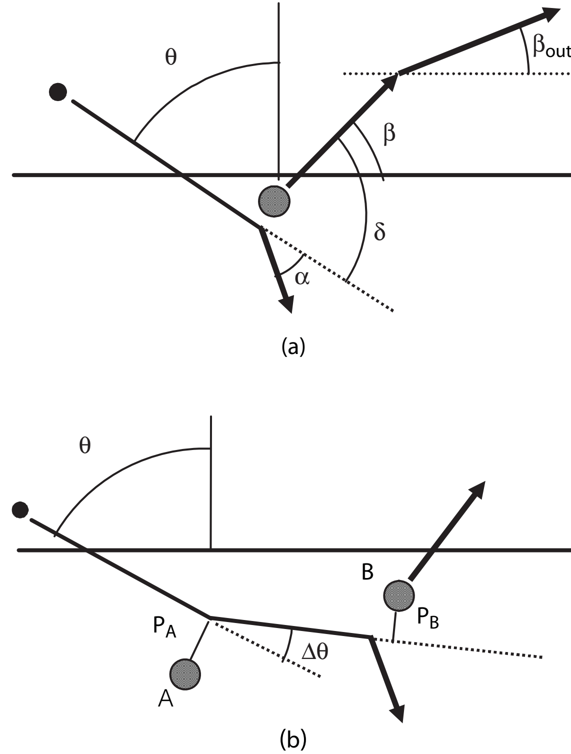

Fig. 1.8. Schematic diagram of knockout processes by light ions for oblique incidence. (**a**) *Direct* knockout process. (**b**) *Indirect* knockout process

result, impulse and deposited energy onto the surface decrease. However the DYACAT and MD yields approach a finite value (≈0.07).

Figure 1.11 illustrates a density distribution of deposited energy at $\theta = 80°$ on the surface, where incident atoms travel from the right side to the left side, and the grid width is 5 Å. A low-deposited energy density for the DYACAT and MD results is seen to expand in the left area. This is caused by complex trajectory development under many-body collisions, resulting in an increase in the deposited energy, which is given by the integration of the deposited energy density. In fact, the deposited energies are 27, 50, and 37 eV for the ACAT, DYACAT, and MD cases. Therefore, enhanced energy deposition by many-body collisions increases sputtering yield. The maximum of the deposited energy density is greater than 1.6 eV Å^{-2} for the MD case, while it is less than 1.6 eV Å^{-2} for the ACAT and the DYACAT cases. In the MD simulation, incident energy of a projectile temporarily changes to potential energy among the surface atoms at an impact point because the atoms behave like a cluster under cohesive potential. This is not considered in the limited-MD calculation by the DYACAT code. As a result, the deposited energy density in the MD case is higher than that in the DYACAT case. Since the highly deposited

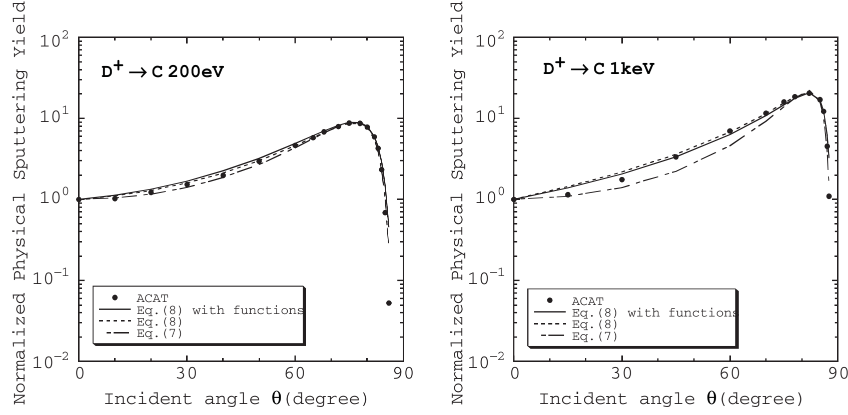

Fig. 1.9. Comparison of the normalized physical sputtering yield vs. incident angle. *Left*: The legend indicates the curves calculated with the three formulae. The *closed circles* are the data obtained with the ACAT code for 200 eV D^+ onto C. *Right*: The caption is the same as in (*left*) except the incident energy is 1 keV. Refer to (*right*) for legend

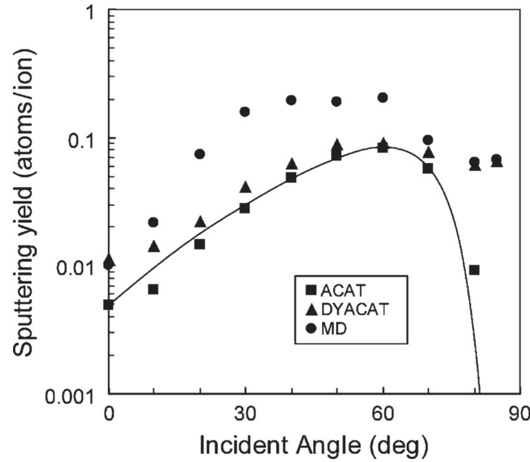

Fig. 1.10. Incident-angle dependence of sputtering yield for 100 eV $W^+ \rightarrow W$. The *solid squares, triangles*, and *circles* indicate the results obtained with the ACAT, DYACAT, and MD codes. The curve shows (1.9) with $A = 1.32$, $f = 3.24$, and $\Sigma = 1.87$

energy density enhances sputtering yield, the MD and DYACAT results are equivalent to grazing incidence, although the deposited energy in the MD case is less than that in the DYACAT case. As indicated in the figure 1.10, this fact influences the yield for incident angles in the range $10° \sim 60°$.

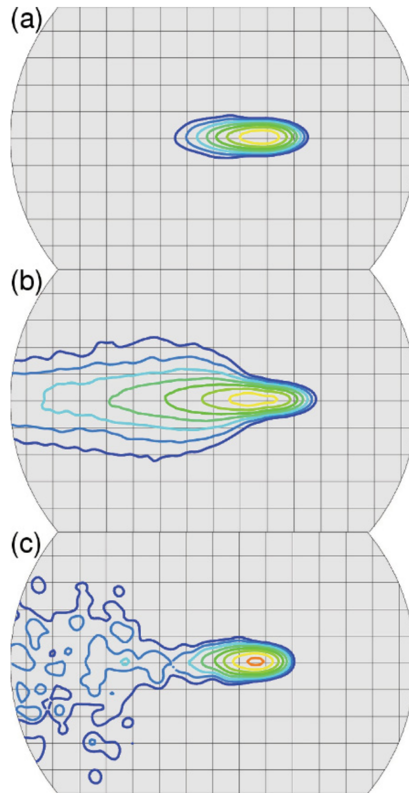

Fig. 1.11. Contour map of deposited energy density on a surface for (**a**) ACAT, (**b**) DYACAT, and (**c**) MD simulations of 100 eV $W^+ \rightarrow W$ at $\theta = 80°$. Incident atoms travel from the right side to the left side. The grid width is 5 Å. The contour lines in eight colors from *dark grey* to *light grey* indicate the densities of 0.003, 0.006, 0.016, 0.04, 0.1, 0.3, 0.6, and 1.6 eV $Å^{-2}$

1.4 Differential Sputtering Yield

While total sputtering yield is required in some cases, differential sputtering yields with respect to energy and ejection angle of sputtered atoms are of importance in other cases. We discuss differential sputtering yields below.

1.4.1 Energy Spectrum of Sputtered Atoms

Quite a large quantity of experimental and calculated data on the energy spectrum of sputtered atoms from solids has been produced and summarized [2, 49–59].

It has been well established experimentally, theoretically, and by computer simulations that an energy spectrum of sputtered atoms coming from a well-developed collision cascade can be well reproduced by *Thompson formula* [60].

Such a developed cascade is generated by high-energy medium-heavy and heavy ions. The formula is expressed in terms of differential sputtering yield $Y(E)$ of atoms sputtered with ejected energy E for incoming ions of normal incidence as

$$Y(E)\mathrm{d}E \propto \frac{\left\{1-\sqrt{(U_\mathrm{s}+E)/\gamma E_0}\right\}}{E^2\left(1+U_\mathrm{s}/E\right)^3}\mathrm{d}E, \tag{1.10}$$

where E_0 and E are the energies of incident ions and sputtered atoms and U_S is the surface binding energy of a target material, $\gamma \equiv 4M_1M_2/(M_1+M_2)^2$, where M_1 and M_2 are the masses of an incoming ion and a target atom. When $\gamma E_0 \gg U_\mathrm{s}, E$, (1.10) is approximated by

$$Y(E)\mathrm{d}E \propto \frac{E}{(E+U_\mathrm{s})^3}\mathrm{d}E. \tag{1.11}$$

As an example, we show in Fig. 1.12 an energy spectrum of sputtered Fe atoms due to 5 keV Ar^+ ion bombardment of normal incidence calculated with the ACAT code, together with the *Thompson formula* [(1.11)]. It is clear from the figure that the formula reproduces the calculated data quite well. Falcone et al. [61] also derived a similar formula. Equation (1.11) indicates that the energy spectrum does not depend on incident energy and angle, and ejection angle. However, more rigorously, it is expected to be dependent on incident energy and angle. The dependence seems to be more prominent for a cohesive material. To be able to discuss the nature of the energy distributions quantitatively, (1.11) should be generalized to have a form,

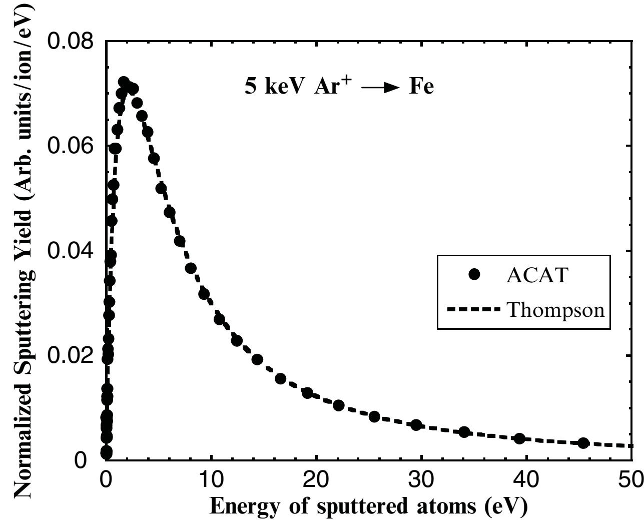

Fig. 1.12. Energy spectrum of Fe atoms due to 5 keV Ar^+ ion bombardment of normal incidence

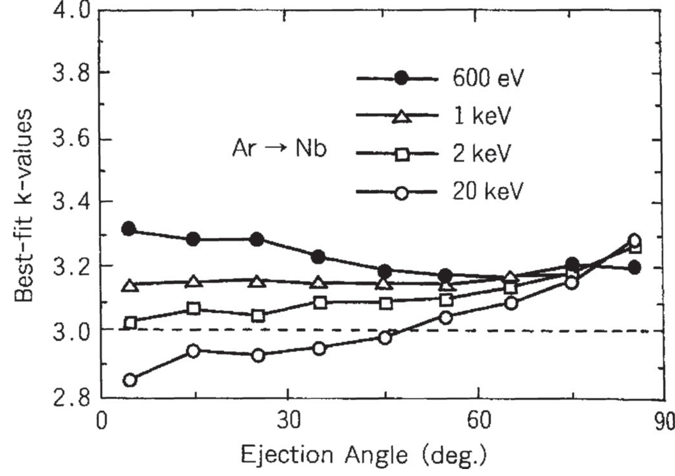

Fig. 1.13. Best-fit values of k in (1.12) applied to the energy distribution of sputtered atoms from Nb irradiated normally by Ar^+ ions with a variety of incident energies

$$Y(E)\mathrm{d}E \propto \frac{E}{(E+U_\mathrm{s})^k}\mathrm{d}E. \tag{1.12}$$

The value of k depends on the interaction potential for elastic collisions. Equation (1.12) peaks at $U_\mathrm{s}/(k-1)$. By computer simulations, we obtained an energy distribution at each ejection angle of sputtered atoms from cohesive Nb ($U_\mathrm{s} = 7.75\,\mathrm{eV}$) irradiated normally by Ar^+ ions with a variety of incident energies. The best-fit value of k was derived by fitting (1.12) with the energy spectra, and potted in Fig. 1.13 as a function of the ejection angle. It is clear from Fig. 1.13 that a variation in k is around $k = 3.0$ with a width ± 0.2. In addition, for less cohesive target materials like Cu, the dependence of k on ejection angle is estimated to be weaker (see for more discussion [62]). Thus, the *Thompson formula* can almost represent energy distributions of sputtered atoms from target materials.

Deviations from the *Thompson formula* have been observed in measurements for incident energy below 1 keV, particularly, for light ions [52–54, 59, 62–66]. The peak of an energy spectrum tends to shift to lower energy and the width of the spectrum becomes narrower. As described in Sect. 1.3.1, the sputtering mechanism II becomes dominant in such a low energy range.

To explain the energy spectrum of sputtered atoms from heavy target materials by low-energy light-ion bombardment, by assuming that sputtered atoms are only primary recoils that undergo only elastic collisions, Falcone [67] derived a formula

$$Y(E_0, E)\mathrm{d}E \propto \mathrm{d}E \frac{E}{(E+U_\mathrm{s})^{5/2}} \ln \frac{\gamma E_0}{E+U_\mathrm{s}}. \tag{1.13}$$

Assuming likewise that light-ion sputtering is mainly due to the primary knock-on atoms, i.e., recoils, produced by ions backscattered from inside the material, Kenmotsu et al. [68] obtained a formula on the basis of the transport theory.

$$Y(E_0, E)\mathrm{d}E \propto \mathrm{d}E \frac{E}{(E+U_\mathrm{s})^{8/5}} \left[\ln \frac{T_\mathrm{max}}{E+U_\mathrm{s}}\right]^2 , \tag{1.14}$$

where $T_\mathrm{max} = \gamma(1-\gamma)E_0$. It is notable that (1.10), (1.13), and (1.14) depend on incident energy of a projectile.

Figure 1.14 illustrates the energy spectra of sputtered atoms calculated with the ACAT code for a Fe target material bombarded normally by 50, 100, and 500 eV D^+ ions, together with (1.11), (1.13), and (1.14). Each spectrum was normalized to unity at the maximum value. Equation (1.14) predicts quite well the energy spectra for 50 and 100 eV D^+ ion bombardment as compared with (1.11) and (1.13). Equation (1.14) differs from the ACAT results for the 500 eV case. The reason for this difference is considered to be due to the neglect

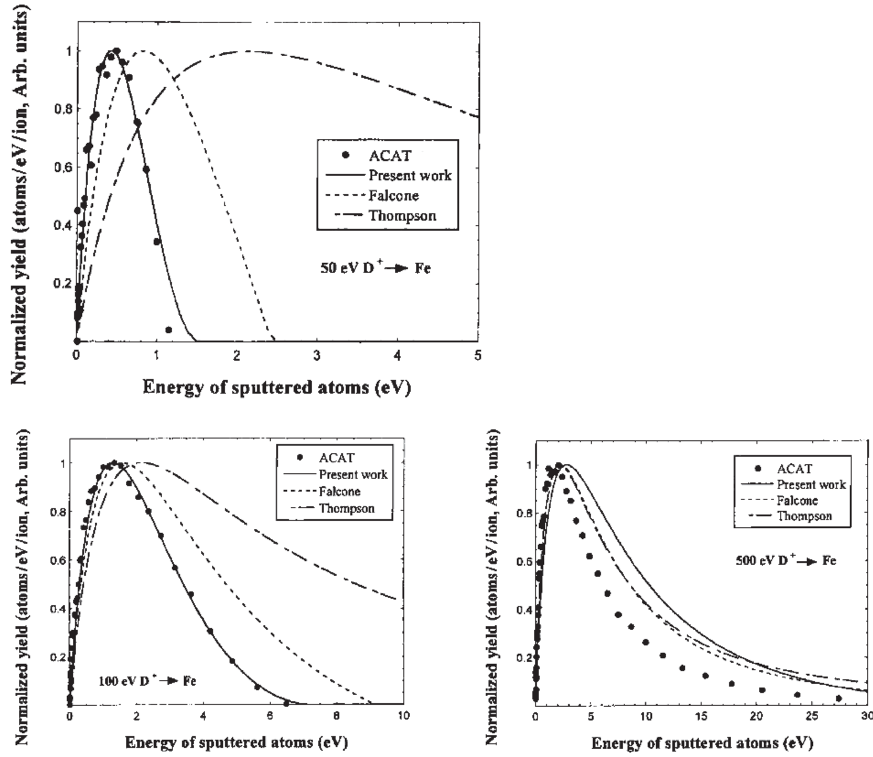

Fig. 1.14. Energy spectra of sputtered atoms calculated with the ACAT for 50, 100, and 500 eV D^+ ions incident normally on a Fe target, together with (1.11), (1.13), and (1.14)

Table 1.3. Peak energies of spectra obtained by fitting (1.11), (1.13) and (1.14) with the ACAT results

Incident energy (eV)	Present work (eV)	Falcone (eV)	Thompson (eV)
50	0.43	0.83	2.14
100	1.29	1.58	2.14
500	2.77	2.22	2.14

of an inelastic energy loss in the model. An inelastic energy loss is dominant for 500 eV, because this energy loss increases in proportion to the projectile's velocity. Therefore, (1.14) is valid for the incident energy of light ions below a few hundred eV. From these figures, the peak position of the ACAT results shows a slight shift toward higher energy as incident energy increases, as pointed out above. Table 1.3 lists peak energies obtained by fitting (1.11), (1.13), and (1.14) with the ACAT results. Both (1.13) and (1.14) indicate that the peak position of the energy spectrum is an increasing function of incident energy. Equation (1.11) is not a function of incident energy. The peak energy of (1.13) is larger than that of (1.14) and the ACAT data for the 50 and 100 eV D^+ cases.

Most recently, Ono et al. [69] extended (1.14) by taking into account an inelastic and elastic energy loss while keeping the same sputtering mechanism as assumed in [68]. In addition, they assumed that primary knock-on atoms produced by backscattered ions do not lose energy while penetrating to the material up to the surface, instead of the energy loss model employed in [68]. The extended formula is expressed in terms of normalized energy-distribution function and fits well with the data calculated with the ACAT code for 50 eV, 100 eV, and 1 keV D^+ ions impinging on a Fe target.

Figure 1.15 shows the energy spectra of sputtered particles for 5 keV Ar^+ ions incident normally on a random surface. The ACAT result is plotted for comparison. The ACAT result is reproduced successfully by a Thompson distribution [60]. In the high-energy range, the MD result agrees with the ACAT result, which suggests that sputtered particles come from a collision cascade. But, sputtered particles with low-energy are considered to come from a thermal spike, and are comprised of many Cu clusters. The latter fact indicates the main difference between the MD and the ACAT results.

It is well known that the flux of particles sputtered from a solid surface bombarded with energetic ions is composed not only of atoms but of molecules and clusters [70]. Compared to the understanding of the properties of monomer emission in sputtering, the understanding of the formation and emission of clusters in energetic ion irradiation is much less incomplete. Both computer simulations and experiments have indicated the importance of fragmentation processes and detailed atomistic mechanism which imparts energy to an aggregation of atoms at the surface and causes its ejection [70–72].

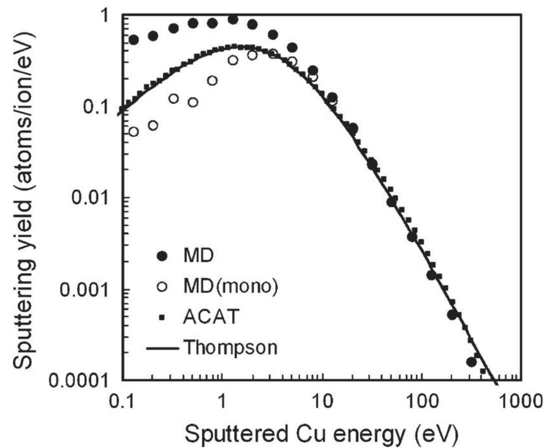

Fig. 1.15. Energy spectra of particles sputtered from a Cu random surface for 5 keV Ar impact. The *circles* and *squares* are the MD and ACAT results. The *open circles* show the monomer yield in the MD result. The *solid curve* is from the approximate Thompson [60] with surface binding energy $U_s = 3.1$ eV

1.4.2 Angular Distribution of Sputtered Atoms

The collision cascade theory predicts that an isotropic distribution of recoil atoms is formed from a well-developed cascade in a target material bombarded normally by energetic projectiles, which results in a cosine-type distribution for the angular distribution of sputtered atoms [20,73]. Experimental data and simulation results indicate that the angular distribution depends on incident energy [74–79]. For low incident energy, a collision cascade is formed, but it is not well developed. As a result, the angular distribution of recoil atoms in the cascade is no longer isotropic, resulting in the angular distribution of ejected atoms being of the under-cosine or heart-shaped type [80]. For high incident energy, on the other hand, an angular distribution tends to become an over-cosine type [75], being different from the cosine shape expected from the collision cascade theory. A qualitative explanation for the over-cosine ejection is that the contribution to sputtering from recoils produced in deeper layers that reach the surface without suffering collisions or that create new recoils (multigenerated) to be sputtered increases as incident energy becomes higher; in this case, the event that the recoil atoms will travel along the direction of the surface normal from the bulk to the surface is highly probable, resulting in an over-cosine distribution [80]. Figure 1.16 shows the types of angular distribution of sputtered atoms, cosine, over-cosine, under-cosine, and heart-shape. The heart-shaped type will be explained later.

The angular distributions of sputtered atoms due to high-energy projectiles can be represented by $\cos^n \theta$, where θ is ejection angle and n is a fitting parameter [75]. Yamamura and Muraoka [78] calculated, with the ACAT code, angular distributions of sputtered recoils produced in the first three atomic

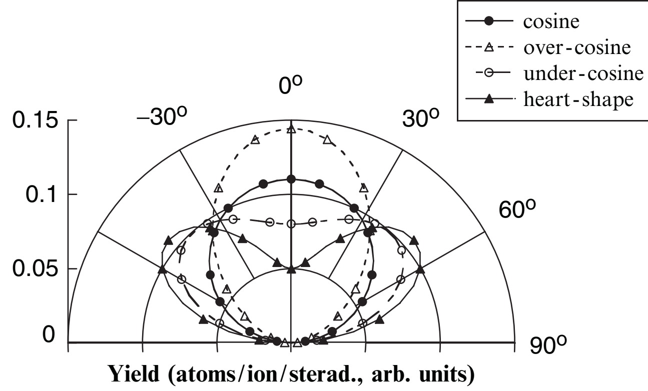

Fig. 1.16. Types of angular distribution of sputtered atom. *Thick solid line*, cosine type; *doted line*, over-cosine type; *dashed-dot line*, under-cosine type; *thin solid line*, heart-shaped type

Table 1.4. Best-fit values of n obtained by fitting $\cos^n \theta$ with experimental data and the calculated angular distributions of sputtered atoms for normal incidence with the ACAT code

Ion	Target	Energy (keV)	Beat-fit n-values				Exp.
			First	Second	Third	Total	
Ar	Fe	0.3	0.64	2.06	4.23	0.67	–
Ar	Fe	0.5	0.87	2.07	4.01	0.97	0.88
Ar	Fe	1.0	1.10	2.58	4.44	1.28	1.0
Ar	Fe	2.0	1.21	2.60	4.33	1.45	1.35
Ar	Fe	3.0	1.28	2.68	4.01	1.53	1.45
Ar	Fe	4.0	1.31	2.63	4.54	1.57	–
Ar	Fe	5.0	1.33	2.65	4.44	1.60	–

layers of a Fe target irradiated normally by 0.3–5 keV Ar^+ ions and derived best-fit values of n for them, as listed in Table 1.4. The best-fit values of n from the first atomic layer derived from the ACAT results are in good agreement with those of experiments, and the degree of the over-cosine distribution, n, is an increasing function of ion energy E. This energy dependence of n is mainly due to the sputtered atoms from the first layer. The angular distribution of sputtered recoils produced at the deeper layers has nearly the same degree of the over-cosine distribution as a function of ion energy. For $E > 1$ keV, the angular distribution from the first layer shows an over-cosine distribution.

Figure 1.17 shows the angular distributions of sputtered atoms for 5 keV Ar^+ ions incident normally on Cu (100), (111), (110) and random surfaces. For the former first three surfaces, the angular distribution has some characteristic peak. From Fig. 1.18, one can see that the spot pattern corresponds to the closed-pack direction of the fcc crystal. The focusing in the

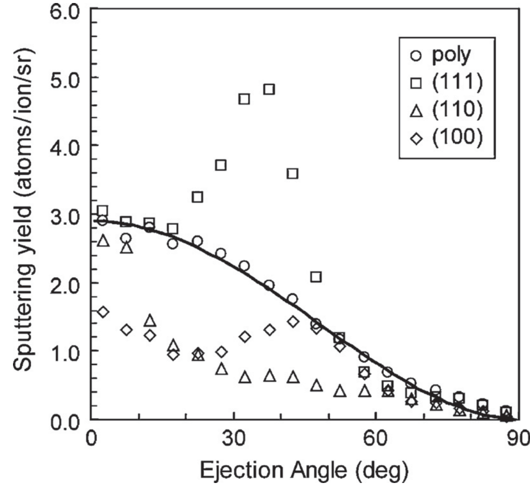

Fig. 1.17. Angular distribution of sputtered atoms for 5 keV Ar^+ impact on a Cu random surface. The *circles, squares, triangles*, and *diamonds* correspond to the results from the random, (111), (110), and (100) surfaces. The *solid curve* is an over-cosine fit $(\cos\theta)^{1.8}$. The ejection angle is measured from the surface normal

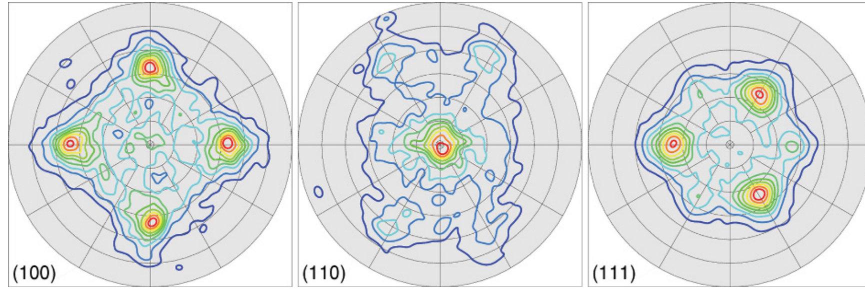

Fig. 1.18. Spot patterns of sputtered Cu atoms for 5 keV Ar^+ impact on Cu (100), (110), and (111) surfaces. Radial and rotational axes correspond to the polar and azimuth angles, respectively. Lines in nine colors from *dark grey* to *light grey* indicate contour lines from 10 to 90% with increment of 10%, of the maximum differential sputtering yield

closed-pack direction causes these peaks. For the random surface, on the other hand, the angular distribution has no characteristic peak and turns out to be of the over-cosine type of $\cos^{1.8}\theta$. This means the effect of the crystal structure disappeared for a random surface.

The following formula can also represent an angular distribution for normal incidence [25, 81, 82]:

$$Y(E,\theta) \propto \cos\theta(1 + B\cos^2\theta), \tag{1.15}$$

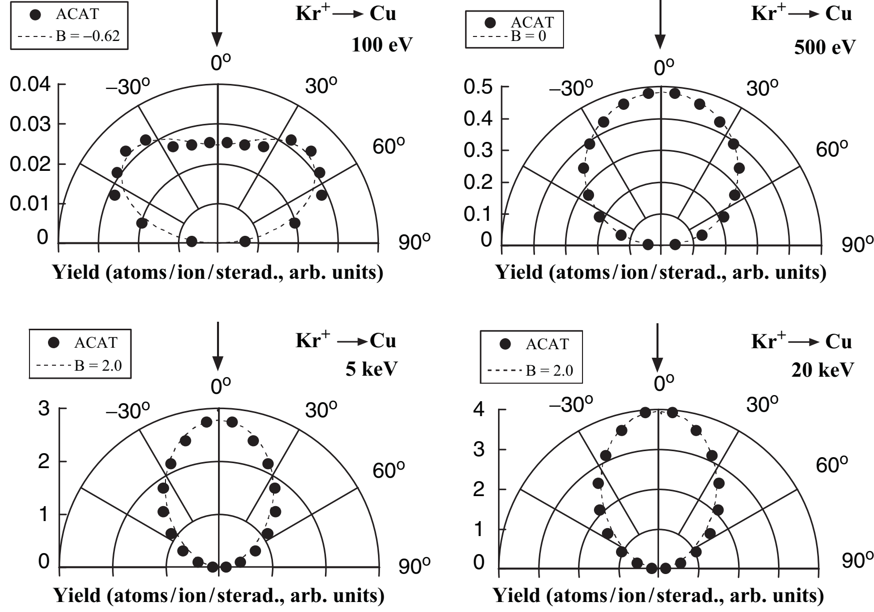

Fig. 1.19. Angular distributions calculated with ACAT for 100 eV, 500 eV, 5 keV Kr^+ ions incident on a Cu target. Also shown are the results of (1.15)

where B is a fitting parameter. The cosine distribution corresponds to $B = 0$ in (1.15). $B > 0$ and $B < 0$ accord with angular distributions of over-, under-cosine, and heart-shaped types, respectively. The fitting function, (1.15), is useful compared with the function $\cos^n \theta$, since (1.15) can describe even a heart-shaped distribution (smaller negative value of B) corresponding to very low incident energy. Figure 1.19 displays angular distributions of sputtered atoms calculated with the ACAT code for 100 eV, 500 eV, 5 keV, and 20 keV Kr^+ ions incident normally on a Cu material. Also shown are the results of the fitting formula [(1.15)]. The best-fit values are $B = -0.62$ for 100 eV, $B = 0$ for 500 eV, $B = 2.0$ for 5 and 20 keV. It is quite clear from the figure that above formula [(1.15)] fits very well with these calculated distributions. The value of B increases with increasing incident energy, except for 5 and 20 keV for which it is the same. Thus, it is not a linear increasing function of incident energy. The behavior of B for incident energies from 5 to 20 keV is understood as: for such high incident energy, since main cascades are formed at great depth from the surface, the recoil density created which is responsible for sputtering becomes nearly constant near the surface, resulting in tending to an isotropic distribution.

The sputtering mechanism for normally incident light ions is described in Sect. 1.3.1, and that for obliquely incident light ions is also presented in Sect. 1.3.2. While an angular distribution formed by the *direct* knockout pro-

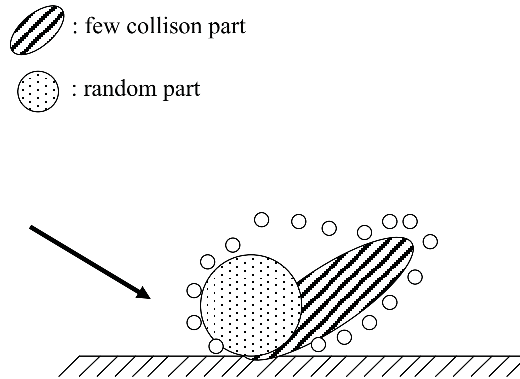

Fig. 1.20. Schematic representation of an angular distribution of sputtered atoms due to light ions of oblique incidence

cess is expected to be narrow, that by the *indirect* knockout process becomes broad, because in the latter case light ions at nearly normal incidence are backscattered nearly isotropic from inside a material. This corresponds to the fact that the angular distribution due to light ions does not lead to the under-cosine type, i.e., cosine or over-cosine types [73]. Therefore, as shown in Fig. 1.20, the angular distribution by light ions of grazing incidence consists of a random and a few collision parts.

Figure 1.21 illustrates the normalized angular distributions of sputtered atoms from a Ni material bombarded by 450 eV and 1 keV H^+ ions at several angles of incidence [39, 75, 76]. The simulation results calculated with ACAT are in good agreement with the experiments except for the case of 450 eV H^+ ions for incident angle 80°. This exception is considered to come from the effect of the surface roughness effect examined and the low incident energy. A comparison of the distribution for normal incidence with that for 60° indicates that, as incident angle becomes larger, a distribution tends to be sensitive to surface roughness, resulting in being broad. Figure 1.22 indicates that the angular distribution by 100 eV H^+ ions incident normally on Cu is the over-cosine type ($B = 0.5$). In contrast, that by 100 eV Kr^+ ions incident on Cu becomes the under-cosine type, as illustrated already in Fig. 1.19. Thus, it is understood that a few collision process characteristic of light-ion bombardment leads to the over-cosine type even in low incident energy.

Assuming sputtering due to the direct knockout process between an incident ion with energy E and a target atom, and planar surface potential U_s, the relation between a recoil angle δ and an ejection angle β_out (see Fig. 1.8) is given as [83]

$$\cos^2 \beta_\mathrm{out} = \frac{\cos^2 \delta \sin^2(\theta + \delta)}{\cos^2 \delta - q^2}, \tag{1.16}$$

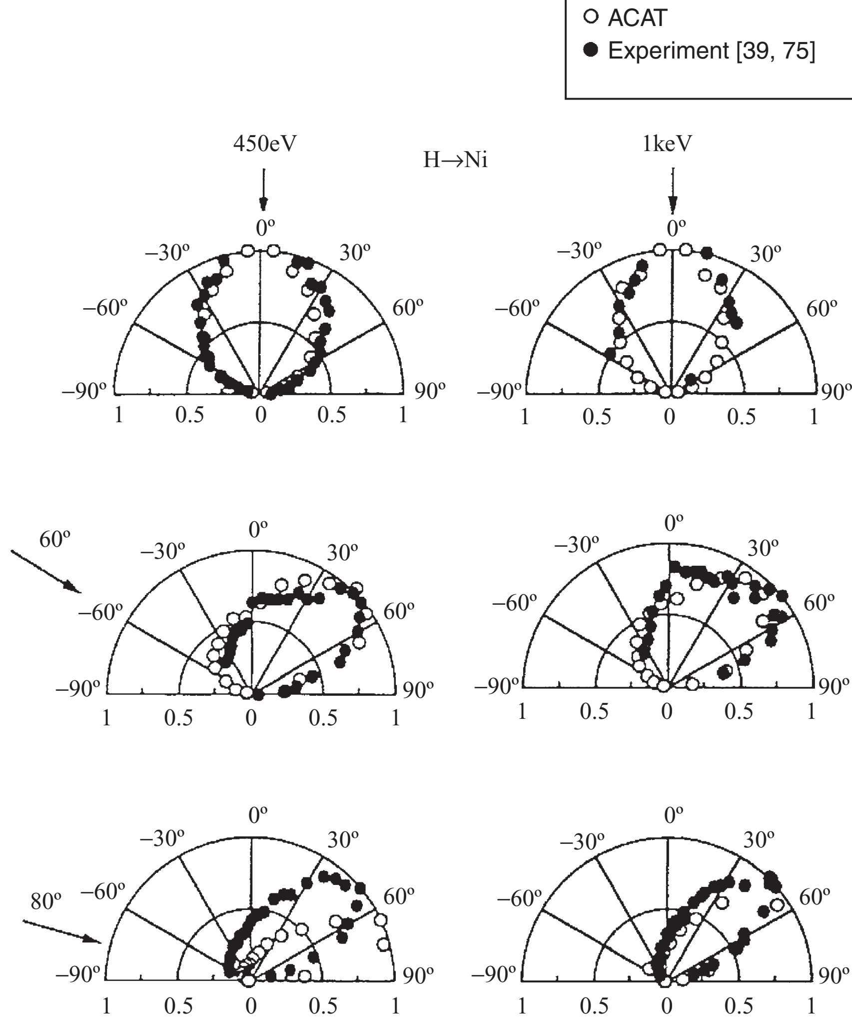

Fig. 1.21. Normalized angular distributions of experimental and ACAT data for 450 eV and 1 keV H^+ ions incident for a Ni material for 0°, 60°, and 80°

where θ is an angle of incidence, $q = \sqrt{U_s/\gamma E}$, $\gamma = 4M_1M_2/(M_1 + M_2)^2$, where M_1 and M_2 are the masses of a projectile and a target atom, respectively. By taking the derivative of (1.16) with respect to δ and set equal to zero, the flowing transcendental equation is obtained:

$$\cos^3\delta\,\cos(\delta + \theta) - q^2\cos(2\delta + \theta) = 0. \tag{1.17}$$

In addition, preferential ejection angle β_p due to the direct knockout process under $q \ll 1$ is roughly given as [79, 83]

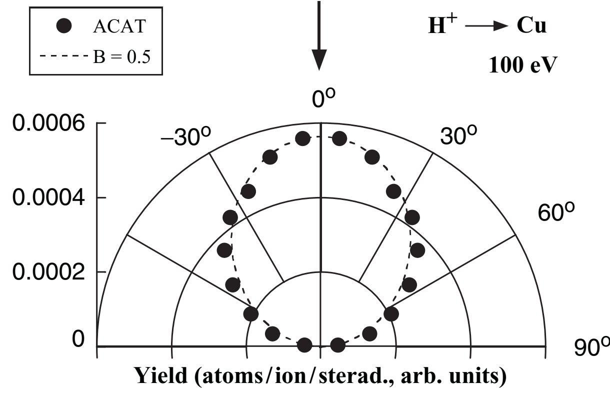

Fig. 1.22. Angular distributions calculated with the ACAT code for 100 eV H^+ ions incident on a Ni target. Also shown are the results of (1.15)

Table 1.5. Comparison with the experimental data and analytical results calculated with (1.18) on the preferential angle β_p

Ion	Target	Energy (keV)	Incident angle (degree)	β_p (degree)	
				Theory (1.18)	Exp.
Ar	Cu	500	80	10.2	∼10.0
Ar	Cu	500	85	5.2	∼5
Ar	Cu	150	85	5.4	∼5
Ar	Cu	900	85	5.2	∼5
Xe	Cu	200	85	5.4	∼5
Ar	Zr	500	80	10.3	∼11
Ar	Zr	500	85	5.3	∼9
Ar	Zr	900	85	5.3	∼8
Ar	Zr	150	85	5.6	∼9
Xe	Zr	200	85	5.5	∼5
H	Ni	0.45	80	46.6	49.3
H	Ni	1	70	45.9	43.0
H	Ni	1	80	33.1	45.0
H	Ni	4	80	32.1	33.7
H	Ni	4	80	21.2	21.0
He	Ni	4	80	15.9°	15.0

$$\beta_p = \cos^{-1}\{(\cos\theta + q)(\cos\theta + 2q)\}^{1/2}. \tag{1.18}$$

Table 1.5 [79] lists the experimental data and analytical results calculated with (1.18) for β_p. Equation (1.18) is in good agreement with the experimental data for the extensive energy range (0.45–500 keV).

Figure 1.23 illustrates the differential sputtering yield of tungsten self-sputtering with incident energy of 100 eV and at $\theta = 30°$, $60°$, and $80°$. Anisotropy was seen for β_p, and β_p increases slightly with increasing inci-

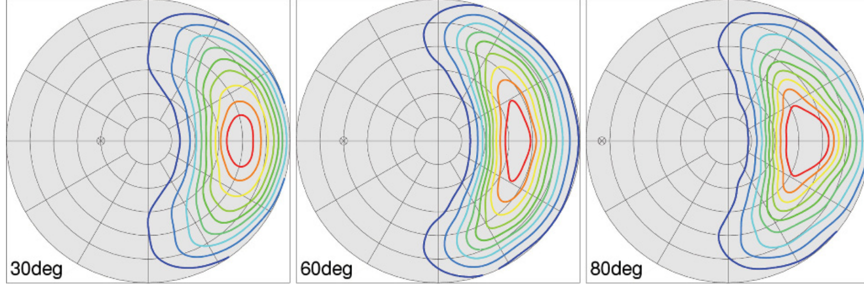

Fig. 1.23. Contour map of differential sputtering yield for 100 eV W $\rightarrow$ W at $\theta = 30^\circ$, 60°, and 80°. The radial and rotational axes correspond to the polar and azimuth angle, respectively. Lines of nine colors from *dark grey* to *light grey* indicate couture lines from 10 to 90% with inclement of 10%, of the maximum differential sputtering yield

dent angle. This result corresponds qualitatively with the feature that (1.18) indicates.

1.5 Sputtering from Rough Surface

It is known that the surface in the BCA code is atomically rough. The random surface in the MD code is also atomically rough. To observe the effect of a surface roughness that is greater than the atomic roughness, we also performed the MD simulations using a fractal surface, which is constructed by the Fourier filtering method [84]. The height z at a horizontal position $\boldsymbol{r} = x\boldsymbol{i}+y\boldsymbol{j}$ is given by the two-dimensional discrete inverse Fourier transform as

$$z(\boldsymbol{r}) = \sum_{k_x=0} \sum_{k_y=0} \{A(\boldsymbol{k})\cos(\boldsymbol{k}\cdot\boldsymbol{r}) + B(\boldsymbol{k})\sin(\boldsymbol{k}\cdot\boldsymbol{r})\}, \qquad (1.19)$$

where $\boldsymbol{k} = k_x\boldsymbol{i} + k_y\boldsymbol{j}$ is the wave vector, the spectral density is $S(\boldsymbol{k}) = A^2(\boldsymbol{k}) + B^2(\boldsymbol{k}) \propto ({k_x}^2 + {k_y}^2)^{D-4}$, and D is the fractal dimension.

Figure 1.24 shows the incident-angle dependence of tungsten self-sputtering yield with incident energy of 1 keV calculated with the MD code. Open circles indicate sputtering yields for the fractal surface with $D = 2.15$ and the RMS roughness of about 2λ, where λ is defined in Sect. 1.2. We found that the rough surface reduces incident-angle dependence because the local surface normal vectors are randomized for the rough surface which is shown in Fig. 1.25a. This is equivalent to randomizing incident angle. The randomization is derived from low wave number components of (1.19) because we should consider the size of the local surface that includes a collision cascade.

In Fig. 1.26, we show, with the ACAT code, the incident-angle dependence of Cu self-sputtering yield with incident energy of 1 keV. From Fig. 1.26, one can find that ions normally incident on rough surfaces ($D = 2.2,\ 2.5$) gives

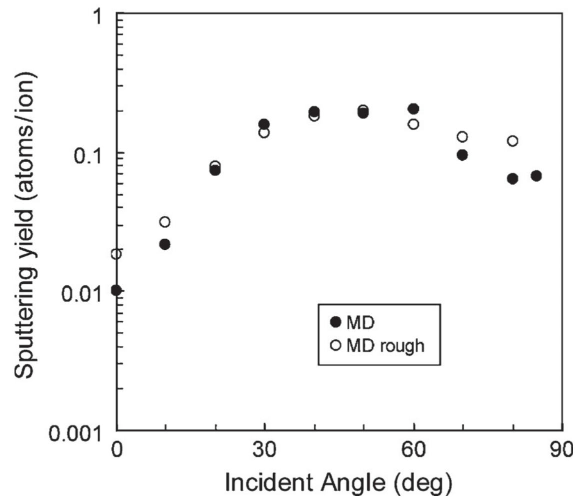

Fig. 1.24. Incident-angle dependence of sputtering yield for 100 eV W → W. The *open circles* correspond to the MD results on a rough surface

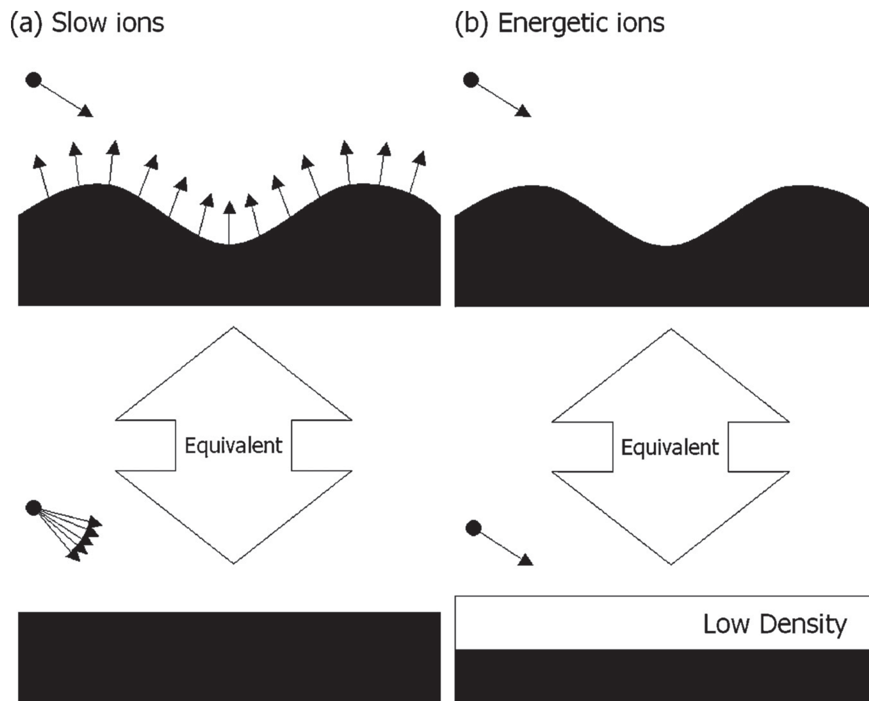

Fig. 1.25. Schemata of rough surface sputtering. (**a**) Low-energy ions incident on a rough surface is equivalent to randomizing incident angle. (**b**) High-energy ions incident on a rough surface is equivalent to a low-density surface

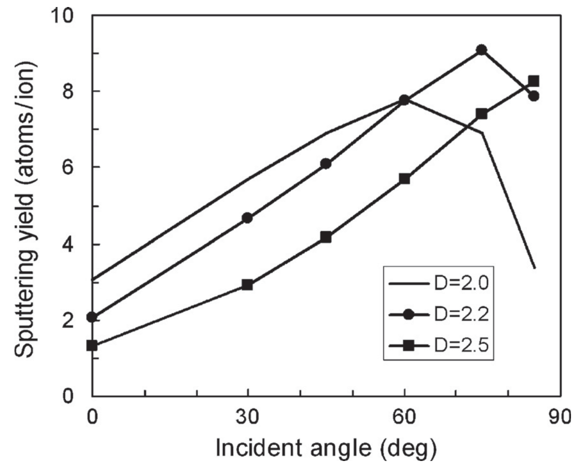

Fig. 1.26. Incident-angle dependence of sputtering yield for 1 keV Cu → Cu with $D = 2.0$, 2.2, and 2.5, respectively

rise to lower sputtering yield than that on a smooth surface ($D = 2.0$). Since a high-energy collision cascade develops in a wide area of the surface, high-energy sputtering is affected by the averaged low-density surface which is schematized in Fig. 1.25b, which reconfirms the results obtained by Kenmotsu et al. [85] about low-density effect of the fractal surface on sputtering. This effect was not found in low-energy sputtering as shown in Fig. 1.24. When a low-energy projectile collides with surface atoms, it is influenced by them, and feels the direction of the local surface normal. Thus, randomization of a surface normal is important for low-energy sputtering.

1.6 Sputtering of Compound Targets

When a multicomponent material is bombarded strongly with an ion beam, near-surface compositional alteration is an unavoidable phenomenon which results from a combination of several kinetic (preferential sputtering, collision mixing, etc.) and thermal processes (radiation-induced diffusion, Gibbsian segregation and radiation-induced segregation, etc.). The driving forces of surface segregation are strain energy and difference in the chemical potentials between the first and the second layers. The former is radiation-induced segregation, and the latter known as Gibbsian segregation. The relative importance of each process depends on an alloy system, the elements, energy and flux of bombarding ions, and irradiation temperature [86].

To analyze the surface change of multicomponent targets under ion bombardment, Auger electron spectroscopy (AES), ion scattering spectroscopy (ISS), Rutherford backscattering spectroscopy (RBS), secondary ion mass spectroscopy (SIMS), and X-ray photoelectron spectroscopy (XPS) are used.

Kimura et al. [87] made an experiment of 6 keV As_2^+ ion implantation on Si wafers and measured the depth profile up to 10 nm with high-resolution RBS. These analytical techniques are useful to estimate surface concentration and the compositional change near a surface, but the real surface concentrations of constituents are possibly different from those measured by respective technique, because of the different resolutions of these techniques. Therefore, it is difficult to estimate the compositional change near the surface under ion bombardment for multicomponent targets experimentally.

At temperatures lower than room temperature, the surface compositional change of most alloys can be explained mainly by kinetic processes, because the time constants of the processes such as the recession speed due to sputtering are much faster than those of thermal processes. At high temperatures, since the time constants of the latter processes are comparable to or longer than those of the former processes, the phenomenon becomes more complex. The first study of bombardment-induced alterations of surface composition at high temperature was carried out on a Cu−Ni alloy by Shimizu et al. [88]. After this work, there were a lot of measurements on surface and/or surface compositional changes in binary alloys by the AES and ISS techniques [89, 90]. Lam et al. [91] measured changes on the surface and surface compositions of Ni–40 at.% Cu alloys at temperatures between 25 and 700°C, using the ISS technique. They found that the steady-state surface composition was noticeably temperature-dependent above 400°C, which was interpreted in terms of the significant contribution of the second atomic layer to the sputtering flux.

There are two typical theoretical approaches to understand alterations of a surface composition. One is an analytical approach which is based on a diffusion equation [92–95] or on a kinetic balance equation [96]. The other approach is Monte Carlo simulation [97–99]. Ho [92] introduced radiation enhanced diffusion into the model proposed by Patterson and Shirm [93]. Wiedersich et al. [94] presented a theory for radiation-induced segregation by introducing a concept of the preferential migration of vacancies and interstitial of a certain atom. Kelly [95] suggested that surface segregation might be important for the interpretation of compositional changes at the surface. Sigmund and his coworker [96] investigated multicomponent sputtering theoretically on the basis of the kinetic balance equation.

For multiple-component targets, total sputtering yields, Y, are defined with its partial sputtering yields of constituents Y_i as follows [86]:

$$Y = \sum_i Y_i \tag{1.20}$$

At sufficiently low temperature, where thermal processes are not important, the ratio of sputtering yields for a binary target is expressed by

$$\frac{Y_1}{Y_2} = \left(\frac{c_1}{c_2}\right)\left(\frac{c'_2}{c'_1}\right), \tag{1.21}$$

where Y_1 and Y_2 are partial sputtering yields of the two constituents, and c_1, c_2, c'_1 and c'_2 are surface concentrations of each element before the ion bombardment and in the steady state. If a change in the surface concentration for a binary target due to sputtering does not occur, the ratio Y_1/Y_2 is equal to unity. The ratio Y_1/Y_2 for a binary target is usually determined from (1.21) by measuring the surface concentrations of constituents before the ion bombardment and in steady state. The measured sputtering yield ratio of alloys is listed in Table 1.6 [100].

A theory of sputtering on multiple component targets was proposed by Sigmund [73,96,101]. Partial sputtering yield of the i-component for a binary infinite medium is given as:

$$Y_i = c_i \Lambda'_i F_\mathrm{D}(E, \theta, 0), \quad i = 1, 2, \tag{1.22}$$

where

$$\Lambda'_i = \Lambda_i \left(\frac{(U)_i}{U_i} \right)^{1-2m_i} \frac{1}{c_i} \frac{G_i}{(G)_i}.$$

Table 1.6. Sputtering yield ratio of alloys. Also listed are atomic weight ratio and ratio of sublimation energies of constituent atoms of pure metals [100]

System (A–B)	Mass ratio $(M_\mathrm{A}/M_\mathrm{B})^{-1}$	Sputtering yield ratio $(Y_\mathrm{A}/Y_\mathrm{B})$	Ration of sublimation energy in eV $(U_\mathrm{A}/U_\mathrm{B})$	Ion	Method and references
Al–Cu	0.42	2.1	3.36/3.52	Xe (1 keV)	RBS [99]
Al_2–Au	0.14	1.9	3.36/3.80	Ar (40 keV)	RBS [100]
Al–Au_2	0.14	1.3	3.36/3.80	Ar (40 keV)	RBS [100]
Si–Ni	0.48	1.6	4.70/4.46	Ar (40 keV)	RBS [100]
Si–Pt	0.14	2.1	4.70/5.86	Ar (40 keV)	RBS [100]
Si–Pt_2	0.14	1.6	4.70/5.86	Ar (40 keV)	RBS [100]
Au–Cr	3.3	1.4–2.0	3.80/4.12	Ar (0.5–2 keV)	AES [101]
Cu–Ni	1.1	1.7	3.52/4.46	Ar (0.5–2 keV)	AES [102]
Cu–Ni	1.1	1	3.52/4.46	Ar (3 keV)	ISS [103]
Ni–Pt	0.3	1.5–1.9	4.46/5.86	Ar (2 keV)	AES [104]
Pd–Ni	1.7	1.5–1.7	3.91/4.46	Ar (0.5–2 keV)	AES [105]
Cu–Pd	0.63	1.5–1.6	3.52/3.91	Ar (2 keV)	AES [106]
Cu–Pt	0.32	1.6–3.0	3.52/5.86	Ar (2 keV)	AES [107]
Cu–Au	0.32	1	3.52/3.80	Ar (1 keV)	AES [107]
Cu_3–Au	0.32	1.1	3.52/3.80	Ar (40 keV)	RBS [100]
Cu_3–Au	0.32	2.3–2.8	3.52/3.80	Ar (0.5–5 keV)	Electron diffraction [108]
Ag–Pd	1.0	1.5–1.6	2.97/3.91	Ar (2 keV)	AES [109]
Au–Pd	2.0	1.0–1.4	3.80/3.91	Ar (2 keV)	AES [109]
Ag–Au	0.56	1.7–1.8	2.97/3.80	Ar (1 keV)	AES [107]
Ag–Au	0.56	1.2	2.97/3.80	Ar (40 keV)	RBS [100]
Ag–Au	0.56	1	2.97/3.80	Ne (1.5 keV)	ISS [110]

Here c_i is atomic concentration of the binary alloy. The relation between c_1 and c_2 is expressed by $c_1 + c_2 = 1$ for the binary alloy. The quantity $F(E, \theta, 0)$ is the deposited energy per unit depth in the alloy surface, m_i exponent in the inter-atomic power law potential for an elemental the i-target, Λ_i a material constant for an elemental i-target, $(U)_i$ surface potential in an elemental i-target, U_i and surface potential for an i-atom of the alloy. The factor $G_i/(G)_i$ is ratio of the flux functions between i-atoms in the alloy and elemental i-target. G_i and $(G)_i$ are densities of moving target atoms in a collision cascade generated by incident ions or recoil atoms for the alloy and an elemental target, respectively. For roughly equal masses M_1, M_2 of the constituents, one may approximate $G_i/(G)_i \approx c_i$.

Using (1.22) and assuming $m_1 = m_2$, the ratio of sputtering yields for the binary alloy is expressed by

$$\frac{Y_1}{Y_2} = \frac{c_1}{c_2} \left(\frac{M_2}{M_1} \right)^{2m} \left(\frac{(U)_2}{(U)_1} \right)^{1-2m} . \tag{1.23}$$

Heat of sublimation is generally taken as an approximate value for surface binding energy of elemental targets [73]. It is difficult to estimate surface binding energy of each element of multiple-component targets, because the energy depends on the surface concentration of the elements and surface coordination numbers. For a random binary alloy the surface binding energy U_1 is derived as a function of surface concentration of the constituents and the nearest-neighboring bond strengths [95, 102]:

$$U_1 = -Z_\mathrm{s}[c_1 U_{11} + c_2 U_{12}], \tag{1.24}$$

where Z_S is surface coordination number, and U_{11} and U_{12} are bond strengths.

To estimate the ion-fluence dependence of depth profiles and compositional changes during ion bombardment, there are several Monte Carlo simulation codes that are based on the BCA. The EVOLVE code was developed by Roush et al. [97]. The TRIDYN was made by Möller and Eckstein [98], and the ACAT-DIFFUSE was proposed by Yamamura [6]. The ACAT-DIFFUSE code calculated compositional changes near a surface and depth profiles in Ni–40 at. % Cu alloys at various temperatures (25–500°C) when sputtering is taking place with normal incident-beam of 3 keV Ne^+ ions [103]. The compositional change near surface calculated with the ACAT-DIFFUSE code is shown below.

As Gibbsian segregation, the ACAT-DIFFUSE code uses the Darken description [104]. The application of the modified Darken equation leads to the following coupled rate equations [103–105]:

$$
\begin{aligned}
\frac{\partial X_1^{\phi}}{\partial t} &= \frac{\Xi_1 X_1^{B_1}}{a_1^2}\left[\frac{\Delta G_1}{RT} + \ln\left\{\frac{X_1^{B_1}\left(1-X_1^{\phi}\right)}{X_1^{\phi}\left(1-X_1^{B_1}\right)}\right\}\right], \\
\frac{\partial X_1^{B_1}}{\partial t} &= \frac{\Xi_1 X_1^{B_2}}{a_2^2}\left[\ln\left\{\frac{X_1^{B_2}\left(1-X_1^{B_1}\right)}{X_1^{B_1}\left(1-X_1^{B_2}\right)}\right\} - \left(\frac{a_2}{a_1}\right)^2 \ln\left\{\frac{X_1^{B_1}\left(1-X_1^{\phi}\right)}{X_1^{\phi}\left(1-X_1^{B_1}\right)}\right\}\right], \\
&\vdots \\
\frac{\partial X_1^{B_i}}{\partial t} &= \frac{\Xi_1 X_1^{B_{i+1}}}{a_{B_{i+1}}^2}\left[\ln\left\{\frac{X_1^{B_{i+1}}\left(1-X_1^{B_i}\right)}{X_1^{B_i}\left(1-X_1^{B_{i+1}}\right)}\right\} - \left(\frac{a_{B_{i+1}}}{a_{B_i}}\right)^2\right. \\
&\qquad \left.\ln\left\{\frac{X_1^{B_i}\left(1-X_1^{B_{i-1}}\right)}{X_1^{B_{i-1}}\left(1-X_1^{B_i}\right)}\right\}\right], \\
&\vdots
\end{aligned}
\tag{1.25}
$$

where X_1^{ϕ} and $X_1^{B_i}$ are fractional concentrations of species 1 in the topmost and the ith layers, respectively. In deriving above equations we use chemical potential terms for an ideal binary alloy, i.e., $\mu = \mu^0 + RT\ln\ X$, where μ^0 is standard chemical potential, R universal gas constant, and T is temperature. The coefficient Ξ_1 corresponds to a diffusion constant given by $\Xi_1 = M_1 RT$. In this model segregation takes place from the bulk B to the surface Φ, because $\mu_1^{0\phi} \neq \mu_1^{0B}$. Segregation energy is given by $\Delta G = \mu_1^{0B} - \mu_1^{0\phi} - {}_2^{0B} + \mu_2^{0\phi}$. Above-coupled equations lead to the Langmuir–McLean relation in a stationary phase [91]

$$
\frac{X_1^{\phi}}{1-X_1^{\phi}} = \frac{X_1^{B}}{1-X_1^{B}} \exp\left[\frac{\Delta G}{kT}\right]. \tag{1.26}
$$

Lam et al. [91] measured the surface compositional change of Ni–40 at.% Cu alloy bombarded normally with flux of 3.75×10^{13} ions cm^{-2} s^{-1} of 3 keV Ne^{+} ions. The simulations were done under the same conditions as the experiments. When the specimen is heated to a high temperature, a thermodynamic driving force gives rise to Cu enrichment at the alloy surface even in the absence of sputtering. Lam et al. gave the following expression for segregation energy ΔG of a Ni–40 at.% Cu ally at high temperature (500°C):

$$
\Delta G = -2.6kT + 0.42. \tag{1.27}
$$

From (1.26) and (1.28), we have the reasonable estimation of the surface atoms fraction Cu$^{\phi}$ and Ni$^{\phi}$ at the topmost layer before ion bombardment which is denoted by [Cu$_x$Ni$_{1-x}$] in the ensuring discussions. In the calculations with ACAT-DIFFUSE we considered only one trap site which is vacancy and the basic diffusion equation is for interstitial diffusion. The respective activation

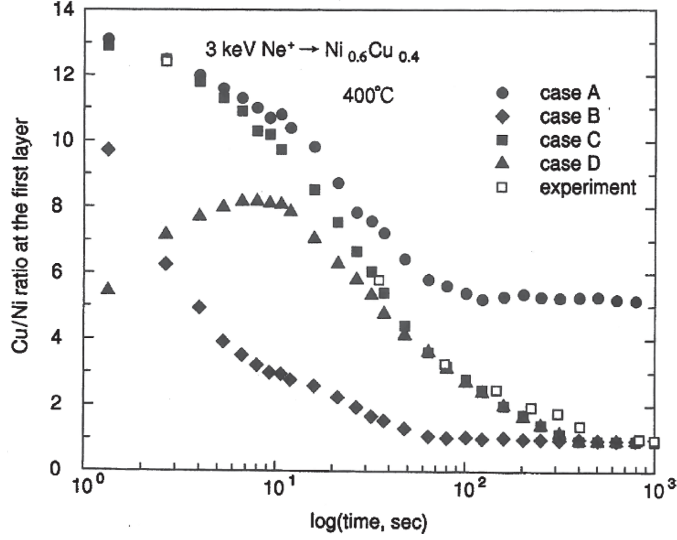

Fig. 1.27. Time evolution of the Cu^{ϕ}/Ni^{ϕ} ratio in the first layer during 3 keV Ne^+ ion sputtering of a Ni–40 at.% Cu alloy at 400°C, where the ion flux is 3.75×10^{13} ions cm^{-2} s^{-1}. *Solid symbols* mean the ACAT-DIFFUSE data and *open symbol* Lam's experimental data [91]. The parameters of cases A, B, C and D are listed in Table 1.7

energies of Ni and Cu are assumed to be 0.93 and 0.88 eV for the interstitial diffusion, and the vacancy diffusion is considered indirectly by solving the rate equation of trapped atoms concentration, where the trapping energies of Ni and Cu are set to be 2.03 and 1.76 eV, respectively. We use smaller detrapping energies than the diffusion activation energies in the material with no irradiation, because trapped atoms may be in an excited state compared with a lattice atom. This leads to the radiation-induced diffusion.

Figure 1.27 shows the calculated Cu^{ϕ}/Ni^{ϕ} ratio in the topmost layer at 400°C as a function of bombarding time. We made simulations for four cases in which the physical parameters used are listed in Table 1.7, where ΔG_0 is the segregation energy before bombardment. Since (1.28) can not be applied to $T < 500°C$, both ΔG_0 and $[Cu_x Ni_{1-x}]$ are determined from the extrapolation of the experimental data [91]. The ion-fluence dependence of Cu^{ϕ}/Ni^{ϕ} ratio of case A is in agreement with the experimental data only at the early stage ($t < 10$ s), and the parameters of case A give the large steady-state Cu^{ϕ}/Ni^{ϕ} ratio compared with the experiment. The segregation speed of case B is very small and it gives good agreement with the experimental steady-state Cu^{ϕ}/Ni^{ϕ} ratio, but the ratio drops more rapidly than the experiment.

There are experimental evidences [106, 107] that segregation energy under irradiation is smaller than that before bombardment. Referring to ion-fluence dependence of the calculated Cu^{ϕ}/Ni^{ϕ} ratios for case A and B, we adopt the

Table 1.7. Initial surface atoms fractions Ξ, ΔG_0, ΔG_S and decay constant τ for cases A, B, C and D

Parameters	Case A	Case B	Case C	Case D
Initial surface atoms fractions	$[Cu_{0.99}Ni_{0.01}]$	$[Cu_{0.99}Ni_{0.01}]$	$[Cu_{0.99}Ni_{0.01}]$	$[Cu_{0.4}Ni_{0.6}]$
Ξ (cm^2 s)	1.0×10^{-15}	3.5×10^{-17}	1.0×10^{-15}	1.0×10^{-15}
ΔG_0 (eV)	0.175	0.175	0.175	0.175
ΔG_{st} (eV)	0.175	0.175	0.050	0.050
τ (ions cm^{-2})	–	–	2.0×10^{16}	2.0×10^{16}

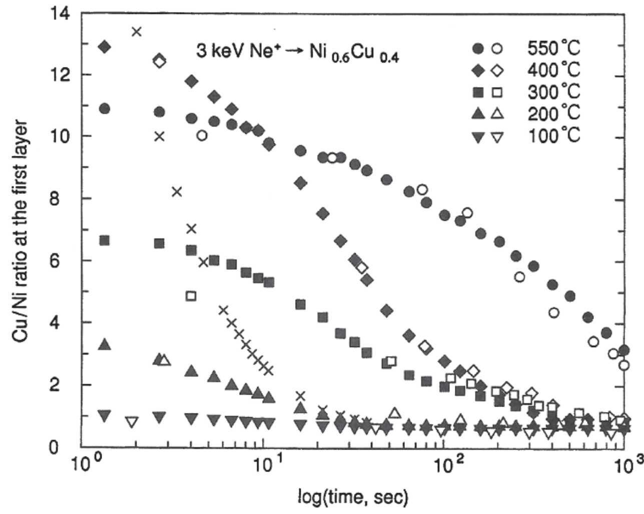

Fig. 1.28. Time evolution of the Cu^{ϕ}/Ni^{ϕ} ratio at first layer during 3 keV Ne^+ ion sputtering of a Ni–40 at.% Cu alloy at various temperatures, where the ion flux is 3.75×10^{13} ions cm^{-2} s^{-1}. *Solid symbols* denote the ACAT-DIFFUSE data and *open symbols* denote Lam's experimental data [91]. The parameters used in the calculation are listed in Table 1.7. The *cross marks* denote the ACAT-DIFFUSE simulation of $T = 100°$C with the initial atom fraction $[Cu_{1.0}Ni_{0.0}]$

following ansatz:

$$\Delta G = \max[\Delta G_0 \exp(-\Phi/\tau), \Delta G_{st}], \tag{1.28}$$

where ΔG_{st} is segregation energy in a steady state. As shown in Fig. 1.27, the ion-fluence dependence of the calculated Cu^{ϕ}/Ni^{ϕ} ratio for case C is in good agreement with the experiment in the whole range considered. To show the dependence of the initial surface atoms fraction on Cu^{ϕ}/Ni^{ϕ} ratio, we use the bulk atoms fraction as an initial surface atoms fraction in case D. Before 50 s, Cu^{ϕ}/Ni^{ϕ} ratio is strongly dependent on the initial surface atoms fraction, but, after 50 s, the Cu^{ϕ}/Ni^{ϕ} ratio shows the same dependence as that of case C.

Table 1.8. Best-fit parameters of the initial surface atoms fractions Ξ, ΔG_0, ΔG_S and decay constant τ for various temperatures

Parameters	Temperature				
	100°C	200°C	300°C	400°C	550°C
Initial surface atoms fractions	[$Cu_{0.4}Ni_{0.6}$]	[$Cu_{0.79}Ni_{0.21}$]	[$Cu_{0.89}Ni_{0.11}$]	[$Cu_{0.99}Ni_{0.01}$]	[$Cu_{0.92}Ni_{0.08}$]
Ξ (cm^2 s^{-1})	2.0×10^{-17}	1.0×10^{-16}	6.0×10^{-16}	1.0×10^{-15}	1.0×10^{-14}
ΔG_0 (eV)	0.003	0.006	0.120	0.175	0.200
ΔG_{st} (eV)	0.003	0.006	0.045	0.050	0.080
τ (ions cm^{-2})	–	–	2.0×10^{16}	2.0×10^{16}	8.0×10^{16}

The Cu^{ϕ}/Ni^{ϕ} ratio calculated with the ACAT-DIFFUSE code at various temperatures is displayed in Fig. 1.28, where solid symbols mean the ACAT-DIFFUSE data and open symbols Lam's experimental data [91]. The parameters used in the calculation are listed in Table 1.8, where ΔG_0 and the initial surface atoms fraction [Cu_xNi_{1-x}] are also determined from the extrapolation of experimental data. In low temperature (<300°C), the time constant of kinetic process or the recession speed due to sputtering is faster than the segregation speed, and so we can reproduce the experimental data without using the ansatz (1.28).

While the time constant of kinetic process is independent of temperature, the segregation speed Ξ is an increasing function of temperature. If we employ the ansatz (1.28), as is presented in Fig. 1.28, we can choose the best-fit parameters which give good agreement with the experimental ion-fluence dependence of the Cu^{ϕ}/Ni^{ϕ} ratio. As a comparison, we calculated the Cu^{ϕ}/Ni^{ϕ} ratio at 100°C, assuming that only Cu atoms are present in the first layer before bombardment. These ACAT-DIFFUSE data are plotted by cross marks in Fig. 1.28. For 3 keV Ne^+ ion bombardment we need more than 2.0×10^{15} ions cm^{-2} s^{-1} before the initial surface conditions do not affect the Cu^{ϕ}/Ni^{ϕ} ratio. This is consistent with the case D result shown in Fig. 1.27.

Figure 1.29 illustrates the flux dependence of Cu^{ϕ}/Ni^{ϕ} ratio during sputtering at 300°C, where the parameters in Table 1.8 were used in the calculation and solid and open symbols mean the ACAT-DIFFUSE data and Lam's experiment data, respectively. The ACAT-DIFFUSE data are in good agreement with the experiment for three fluxes. The steady-state Cu^{ϕ}/Ni^{ϕ} ratio of high flux (1.88×10^{14} ions cm^{-2} s^{-1}) indicates a slightly small value, because the kinetic process is strong compared with the other two fluxes.

1.7 Conclusion

We have given a quantitative account of and highlighted the results on sputtering obtained mainly with our computer codes, together with semi-empirical formulas that well reproduce the results.

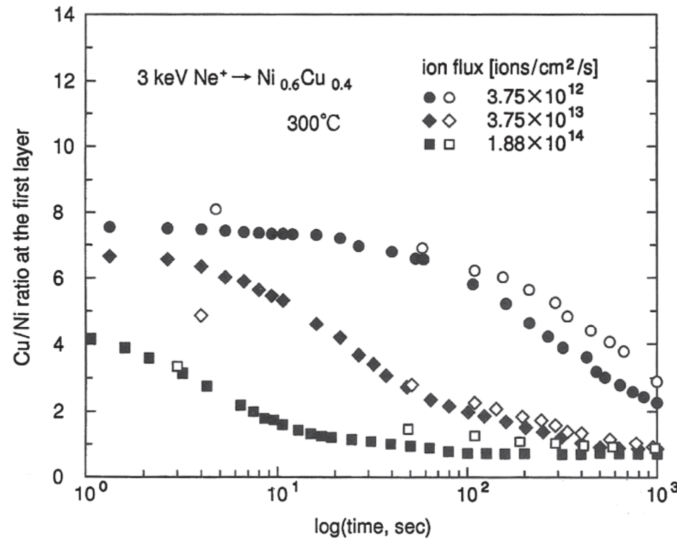

Fig. 1.29. Flux-dependence of the Cu^{ϕ}/Ni^{ϕ} ratio during 3 keV Ne^{+} ion sputtering of a Ni–40 at.% Cu alloy at 300°C, where the ion flux is 3.75×10^{13} ions cm^{-2} s^{-1}. *Solid symbols* indicate the ACAT-DIFFUSE data and *open symbols* indicate Lam's experimental data [91], and the used parameters are listed in Table 1.4

After having described a brief outline of our computer codes in Sect. 1.2, we have mentioned in Sect. 1.1.3 dependences on incident energy and incident angle of total sputtering yield, together with corresponding semi-empirical formulas. The large difference found at glancing angles of incidence between the MC and the MD data was accounted for using the contour maps of deposited energy density on the surface calculated in these simulations.

We have described differential sputtering yield in sputtered energy and ejection angle in Sect. 1.1.4. We have shown that the semi-empirical formulas agree well with the energy spectrum of sputtered atoms from heavy target materials with low-energy light ions. The difference in the angular distributions for heavy- and light-ion bombardment was described. We have also introduced a new semi-empirical formula that represents even the heart-shaped angular distribution due to very low-energy heavy- and moderately heavy-atom bombardment.

In Sect. 1.1.5, we have mentioned the effect of surface roughness on sputtering with low- and high-energy ions. Low-energy ions incident on a rough surface is equivalent to randomizing incident angle, and sputtering with high-energy ions is affected by the averaged effective low-density of a rough surface.

In Sect. 1.1.6, we have treated sputtering of compound materials. We have pointed out that kinetic and thermal processes occurring in a material result in the compositional change. Ion-fluence dependence of the compositional change for a Cu−Ni alloy was calculated with the ACAT-DIFFUSE code where both kinetic and thermal processes are taken into account.

Acknowledgments. The authors are greatly indebted to the theoretical work and computer simulations done by late Prof. Y. Yamamura. They would like to thank Emeritus Prof. T. Kawamura for suggesting valuable comments and encouraging them to complete this work. This work was partly supported by a Grant-in-Aid of the Academic Frontier Project and KAKENHI (19055005) by the Ministry of Education, Culture, Sports, Science, and Technology of Japan.

References

1. H.H. Andersen, Nucl. Instr. Methods B **18**, 321 (1987)
2. W. Eckstein, *Computer Simulation of Ion-Solid Interaction*, Springer Series in Materials Science, vol. 10 (Springer, Berlin Heidelberg New York, 1991)
3. R. Smith, *Atomic and Ion Collisions in Solids and at Surfaces* (Cambridge University Press, Cambridge, 1997)
4. T. Ono, T. Kawamura, T. Kenmotsu, S.T. Nakagawa, T. Muramoto, a manuscript being prepared for submission
5. W. Takeuchi, Y. Yamamura, Radiat. Eff. **71**, 53 (1983); Y. Yamamura, Y. Mizuno, IPPJ-AM-40, Nagoya University, 1985
6. Y. Yamamura, Nucl. Instr. Methods B **28**, 17 (1987)
7. Y. Yamamura, Nucl. Instr. Methods B **33**, 493 (1988)
8. K. Yorizane, T. Muramoto, Y. Yamamura, Nucl. Instr. Methods B **153**, 292 (1999); T. Muramoto, T. Kenmotsu, Nucl. Instr. Methods B **255**, 214 (2007)
9. J.P. Biersack, W. Eckstein, Appl. Phy. A **34**, 73 (1984); K.H. Möller, J. Appl. Phys. **61**, 2516 (1987)
10. K.L. Wilson, M.I. Baskes, J. Nucl. Mater. **76/77**, 291 (1978)
11. L. Verlet, Phys. Rev. **159**, 98 (1967)
12. H.J.C. Berendsen, J.P.M. Postma, W.F. van Gunsteren, A. DiNola, J.R. Haak, J. Chem. Phys. **81**, 3684 (1984)
13. N. Matsunami, Y. Yamamura, Y. Itikawa, N. Itoh, Y. Kazumata, S. Miyagawa, K. Morita, R. Shimizu, H. Tawara, At. Data Nucl. Data Tables **31**, 1 (1984)
14. W. Eckstein, C. Garcia-Rosales, J. Roth, W. Ottenberger, Max-Planck-Institut für Plasmaphysik, IPP 9/82 (1993)
15. E.W. Thomas, R.K. Janev, J. Botero, J.J. Smith, Yanghui Qiu, INDC (NDS)-28 (1993)
16. Y. Yamamura, K. Sakaoka, H. Tawara, Research Report of National Institute for Fusion Science, NIFS-DATA-31 (1995)
17. Y. Yamamura, H. Tawara, At. Data Nucl. Data Tables **62**(2), 149 (1996)
18. W. Eckstein, J.A. Stephens, R.E.H. Clark, J.W. Davis, A.A. Haasz, E. Vietzke, Y. Hirooka, in *Atomic and Plasma-Material Interaction Data for Fusion*, vol. 7, Part B, IAEA, Vienna, 2001
19. W. Eckstein, Max-Planck-Institut für Plasmaphysik, IPP 9/132 (2002)
20. P. Sigmund, Phys. Rev. **184**, 383 (1969); Phys. Rev. **187**, 768 (1969)
21. R. Weissmann, R. Behrisch, Radiat. Eff. **19**, 69 (1973)
22. R. Behrisch, G. Maderlechner, B.M.U. Scherzer, M.T. Robinson, Appl. Phys. **18**, 391 (1981)
23. U. Littmark, S. Fedder, Nucl. Instr. Methods **194**, 607 (1982)
24. Y. Yamamura, N. Matsunami, N. Itoh, Radiat. Eff. **71**, 65 (1983)
25. Y. Yamamura, Radiat. Eff. **55**, 49 (1981)

26. J. Lindhard, M. Scharff, Phys. Rev. **124**, 128 (1961)
27. J. Bohdansky, Nucl. Instr. Methods B **2**, 587 (1984)
28. C. García-Rosales, W. Eckstein, J. Roth, J. Nucl. Mater. **218**, 8 (1994)
29. M.A. Karolewski, Radiat. Eff. Def. Solids **153**, 239 (2001)
30. G. Moliere, Z. Naturforsch A **2**, 133 (1947)
31. J.E. Lennard, I. Jones, Proc. R. Soc. Lond. A **106**, 441, 463 (1924)
32. O.B. Firsov, Sov. Phys. JETP **36**, 1076 (1959)
33. Th.J. Colla, H.M. Urbassek, A. Wucher, C. Staudt, R. Heinrich, B.J. Garrison, C. Dandachi, G. Betz, Nucl. Instr. Methods B **143**, 284 (1998)
34. H.E. Roosendaal, in *Sputtering by Particle Bombardment I*, ed. by R. Behrisch (Springer, Berlin Heidelberg New York, 1981) p. 219
35. T. Ono, T. Kawamura, K. Ishii, Y. Yamamura, J. Nucl. Mater. **232**, 52 (1996)
36. Y. Yamamura, M. Ishida, Appl. Surf. Sci. **203, 204**, 62 (2003); G. Betz, G.K. Wehner, in *Sputtering by Particle Bombardment* vol. II, ed. by R. Behrisch (Springer, Berlin Heidelberg New York, 1983) p. 11
37. G.K. Wehner, J. Appl. Phys. **30**, 1762 (1959)
38. H.L. Bay, J. Bohdansky, Appl. Phys. **19**, 421 (1979)
39. J. Bohdansky, G.L. Chen, W. Eckstein, J. Roth, B.M.U. Scerzer, J. Nucl. Mater. **111, 112**, 717 (1982)
40. W. Eckstein, J. Biersack, Nucl. Instr. Methods B **2**, 550 (1984)
41. A.A. Haasz, J.W. Davis, C.H. Wu, J. Nucl. Mater. **162, 164**, 915 (1989)
42. J. Roth, J. Bohdansky, W. Ottenberger, J. Nucl. Mater. **165**, 193 (1989)
43. Y. Yamamura, Y. Itikawa, N. Itoh, IPPJ-AM-26, Nagoya University, 1983; Y. Yamamura, Radiat. Eff. **80**, 57 (1984)
44. W. Eckstein, R. Preuss, J. Nucl. Mater. **320**, 209 (2003)
45. W. Eckstein, Nucl. Instr. Methods B **232**, 108 (2005)
46. Y. Yamamura, Nucl. Instr. Methods B **2**, 578 (1984)
47. Y. Yamamura, T. Takiguchi, Z. Li, Kakuyugokenkyu **66/3 222**, 277 (1991) (in Japanese)
48. T. Ono, K. Shibata, T. Kenmotsu, T. Muramoto, Z. Li, T. Kawamura, J. Nucl. Mater. **363–365**, 1266 (2007)
49. M.W. Thompson, Phys. Rep. **69**(4), 335 (1981)
50. E. Hintz, D. Rusbüldt, B. Schweer, J. Bohdansky, J. Roth, A.P. Martinelli, J. Nucl. Mater. **93, 94**, 656 (1982)
51. H.L. Bay, B. Schweer, P. Bogen, E. Hintz, J. Nucl. Mater. **111, 112**, 732 (1982)
52. H.L. Bay, W. Berres, E. Hintz, Nucl. Instr. Methods **194**, 555 (1984)
53. H.L. Bay, W. Berres, Nucl. Instr. Methods B **2**, 606 (1984)
54. H.L. Bay, Nucl. Instr. Methods B **18**, 430 (1987)
55. M.W. Thompson, Nucl. Instr. Methods B **18**, 411 (1987)
56. W.O. Hofer, in *Sputtering by Particle Bombardment III*, ed. by R. Behrisch, K. Wittmaack (Springer, Berlin Heidelberg New York, 1991) p. 15
57. G. Betz, K. Wien, Int. J. Mass Spectrom. Ion Proc. **140**, 1 (1994)
58. W. Eckstein, R. Dohmen, H. Friedrich, F. Hertweck, Nucl. Instr. Methods B **153**, 345 (1999)
59. A. Goehlich, N. Niemöller, H.F. Döbele, J. Nucl. Mater. **266–269**, 501 (1999)
60. M.W. Thompson, Philos. Mag. **18**, 377 (1968)
61. G. Falcone, P. Sigmund, Appl. Phys. **25**, 307 (1981)
62. J. Dembowski, H. Oechsner, Y. Yamamura, M. Urbassek, Nucl. Instr. Methods B **18**, 464 (1987)

63. R.V. Stuart, G.K. Wehner, J. Appl. Phys. **35**, 1819 (1964)
64. H. Oechsner, L. Reichert, Phys. Lett. **23**, 90 (1966)
65. H. Oechsner, Phys. Rev. Lett. **24**, 583 (1970)
66. R.A. Brizzolara, C.B. Cooper, Nucl. Instr. Methods B **43**, 136 (1989)
67. G. Falcone, Surf. Sci. **187**, 212 (1987)
68. T. Kenmotsu, Y. Yamamura, T. Ono, T. Kawamura, J. Plasma and Fus. Res. **80**(5), 406 (2004)
69. T. Ono, Y. Aoki, T. Kawamura, T. Kenmotsu, Y. Yamamura, J. Nucl. Mater. **975–979**, 337 (2005)
70. H. Gnaser, *Low-Energy Ion Irradiation of Solid Surfaces*, Springer Tracts in Modern Physics, vol. 146 (Springer, Berlin Heidelberg New York, 1999)
71. T. Muramoto, M. Okai, Y. Yamashita, K. Yorizane, Y. Yamamura, Nucl. Instr. Methods B **180**, 222 (2001)
72. T. Muramoto, Y. Yamamura, Appl. Surf. Sci. **203, 204**, 143 (2003)
73. P. Sigmund, in: *Sputtering by Particle Bombardment*, vol. I, ed. by R. Behrisch, (Springer, Berlin Heidelberg New York, 1981) p. 9
74. G.K. Wehner, D. Rosenberg, J. Appl. Phys. **31**, 177 (1960)
75. J. Roth, J. Bohdansky, W. Ottenberger, Max-Planck-Institut für Plasmaphysik, IPP 9/26, (1979)
76. Y. Yamamura, in *Ionbiimukogaku*, ed. by F. Fujimoto, K. Komaki (Uchida Rokakuho, Tokyo, 1995) p. 239
77. H.H. Andersen, B. Stenum, T. Sørensen, H.J. Whitlow, Nucl. Instr. Methods B 6, 459 (1985)
78. Y. Yamamura, K. Muraoka, Nucl. Instr. Methods B **42**, 175 (1989)
79. Y. Yamamura, C. Mössner, H. Oeschner, Radiat. Eff. **105**, 31 (1987); Y. Yamamura, T. Takiguchi, H. Tawara, NIFS-DATA-1, National Institute for Fusion Science, 1990
80. H.H. Andersen, Nucl. Instr. Methods B **33**, 466 (1988)
81. Y. Yamamura, T. Takiguchi, M. Ishida, Rad. Eff. Def. Solids **118**, 237 (1991)
82. T. Takiguchi, M.Sc. Dissertation, Okayama University of Science, 1989 (in Japanese)
83. Y. Yammaura, Radiat. Eff. **80**, 193 (1984)
84. M.F. Barnsley, R.L. Devaney, B.B. Mandelbrot, H.O. Peitgen, D. Saupe, R.F. Voss, in *The Science of Fractal Images* (Springer, Berlin Heidelberg New York, 1988)
85. T. Kenmotsu, Y. Yamamura, T. Muramoto, N. Hirotani, Nucl. Instrum. Methods B **228**, (2005) 369
86. G. Betz, G.K. Wehner, in *Sputtering by Particle Bombardment*, vol. II, ed. by R. Behrisch (Springer, Berlin Heidelberg New York, 1983)
87. K. Kimura, Y. Oota, K. Nakajima, M. Suzuki, T. Aoki, J. Matsuo, A. Agarwal, B. Freer, A. Stevenson, M. Ameen, Nucl. Instr. Methods B **211**, 206 (2003)
88. H.Shimizu, M. Ono, K. Kawamura, J. Appl. Phys. **46**, 460 (1975)
89. L.E. Rehn, H. Wiedersich, Thin. Solid. Films **73**, 139 (1980)
90. R.S. Li, T. Koshikawa, K. Goto, Surf. Sci. **121**, 1561 (1982)
91. N.Q. Lam, H.A. Hoff, H. Wiedersich, L.E. Rehn, Surf. Sci. **149**, 517 (1985)
92. P.S. Ho, Surf. Sci. **72**, 253 (1978)
93. L. Patterson, G.A. Shirm, J. Vac. Sci. Technol. **4**, 343 (1967)
94. H. Wiedersich, P.R. Okamoto, N.Q. Lam, J. Nucl. Mater. **83**, 98 (1979)
95. R. Kelly, Surf. Sci. **100**, 85 (1980)